HAL open science

Variability of carbonate isotope signatures in a hydrothermally influenced system: insights from the Pastos Grandes caldera (Bolivia).

Cédric Bougeault, Christophe Durlet, Emmanuelle Vennin, Elodie Muller, Magali Ader, Bassam Ghaleb, Emmanuelle Gérard, Aurélien Virgone, Eric C. Gaucher

To cite this version:

Cédric Bougeault, Christophe Durlet, Emmanuelle Vennin, Elodie Muller, Magali Ader, et al.. Variability of carbonate isotope signatures in a hydrothermally influenced system: insights from the Pastos Grandes caldera (Bolivia).. Minerals, 2020, 10 (11), pp.989. 10.3390/min10110989 . hal-03004450

HAL Id: hal-03004450

https://hal.science/hal-03004450v1

Submitted on 18 Jan 2021

HAL is a multi-disciplinary open access archive for the deposit and dissemination of scientific research documents, whether they are published or not. The documents may come from teaching and research institutions in France or abroad, or from public or private research centers.

L'archive ouverte pluridisciplinaire **HAL**, est destinée au dépôt et à la diffusion de documents scientifiques de niveau recherche, publiés ou non, émanant des établissements d'enseignement et de recherche français ou étrangers, des laboratoires publics ou privés.

Distributed under a Creative Commons Attribution - NonCommercial 4.0 International License

minerals

MDPI

Article

Variability of Carbonate Isotope Signatures in a Hydrothermally Influenced System: Insights from the Pastos Grandes Caldera (Bolivia)

Cédric Bougeault [1,*], Christophe Durlet [1], Emmanuelle Vennin [1], Elodie Muller [2], Magali Ader [2], Bassam Ghaleb [3], Emmanuelle Gérard [2], Aurélien Virgone [4] and Eric C. Gaucher [4]

1 Biogéosciences, UMR 6282 CNRS, Université Bourgogne Franche-Comté, 6 boulevard Gabriel, 21000 Dijon, France; christophe.durlet@u-bourgogne.fr (C.D.); emmanuelle.vennin@u-bourgogne.fr (E.V.)
2 Institut de physique du globe de Paris, Université de Paris, CNRS, F-75005 Paris, France; elodie.muller@upmc.fr (E.M.); ader@ipgp.fr (M.A.); emgerard@ipgp.fr (E.G.)
3 Geotop, University of Québec at Montréal, C.P. 8888, Succ. Centre-ville, Montréal, QC H3C 3P8, Canada; ghaleb.bassam@uqam.ca
4 TOTAL CSTJF, Avenue Larribau, CEDEX, 64018 Pau, France; aurelien.virgone@total.com (A.V.); eric.gaucher@total.com (E.C.G.)
* Correspondence: cedric.bougeault@u-bourgogne.fr; Tel.: +33-380396371

Received: 28 August 2020; Accepted: 31 October 2020; Published: 7 November 2020

Abstract: Laguna Pastos Grandes (Bolivia), nesting in a volcanic caldera, is a large, palustrine-to-lacustrine system fed by meteoric and hydrothermal calco–carbonic fluids. These different fluid inputs favor a complex mosaic of depositional environments, including hydrothermal springs, pools, and an ephemeral lake, producing abundant present-day carbonates developing over a Holocene carbonate crust dated by U–Th. Present-day carbonates (muds, concretions, and microbialites) recorded a large range of isotope variations, reaching 13.9‰ in $\delta^{13}C$ and 11.1‰ in $\delta^{18}O$. Sedimentological and geochemical data indicated that the main processes influencing the isotope record were: (i) rapid CO_2 degassing and temperature decreases along hydrothermal discharges; (ii) strong evaporation favored by the arid high-altitude Andean climate, locally enhanced by capillary water rise within microbial mats or by wind-induced spray falling on vadose concretions. Unlike past or present perennial lake systems in Central Andes, the short residence time of brine waters in the ephemeral central lake prevents enrichment of lacustrine carbonates in ^{13}C and ^{18}O. The very low fraction modern $F^{14}C$ in these present-day carbonates demonstrates that incorporation of fossil magmatic carbon related to the volcanic context also prevents any radiocarbon dating. The use of isotopes for the interpretation of ancient continental series should always be accompanied by a thorough characterization of the environmental setting.

Keywords: carbonates; lacustrine; hydrothermal; stable isotopes; spatial analysis; Altiplano

1. Introduction

In continental settings, carbonate mineralization can occur in many environments, fed by different types of parent waters. In fossil contexts, $\delta^{18}O$ and $\delta^{13}C$ from continental carbonates (shells, tufas, speleothems, microbialites, and lacustrine muds) may help to reconstruct paleoclimate and paleohydrology, especially when coupled with dating (e.g., [1–6]). However, interpreting $\delta^{18}O$ and $\delta^{13}C$ from carbonates ($\delta^{18}O_{carb}$ and $\delta^{13}C_{carb}$) is problematic when the isotope source (e.g., magmatic, atmospheric, or biogenic CO_2; hydrothermal versus meteoric H_2O) and other environmental factors affecting the system (e.g., climate, endoreic versus exoreic, kinetic versus biological) cannot be constrained.

The Central Andes (South America, Andean Cordillera) is a region where the absence of long series of peat, continental ice, or speleothems, encourages the use of lacustrine carbonate series to reconstruct climatic and hydrological changes during the Quaternary. The most remarkable example of ancient lakes in the Central Andes is the Altiplano Basin, where several lake highstands, covering a large part of the watershed, occurred in wet periods during the Late Pleistocene. These lake highstands have been identified by the presence of abundant calcitic bioherms that mark paleoshores, now several meters above the modern shoreline of Salar de Uyuni [7]. Previous studies documenting $\delta^{18}O$ and $\delta^{13}C$ in carbonates from ancient Andean lake deposits provide evidence of changes in the hydrological balance, and of volcanic influence during the Pleistocene and the Holocene (e.g., [3,4,8,9]).

Modern Andean analogs can provide key case studies, if hydrochemical and depositional settings are well documented, for better understanding of the processes affecting $\delta^{18}O_{carb}$ and $\delta^{13}C_{carb}$. In this region, the ephemeral or perennial lakes are generally characterized by evaporite, clastic, or diatom deposits, but pure carbonate deposits are lacking [10]. So far, few studies have investigated modern carbonate facies or carbonate stable isotope composition in lacustrine, palustrine, and hydrothermal environments in the Central Volcanic Zone (Figure 1A). Detailed descriptions of such modern carbonates mainly concern the Laguna Negra in Argentina [9,11] and some parts of the Laguna Pastos Grandes in Bolivia [12–14]. Other examples of modern carbonate mineralization have been identified in some Argentinean lakes but without detailed facies analysis or isotope characterization [15]. Laguna Pastos Grandes is a lacustrine-to-palustrine system, extending over 120 km^2 with abundant modern carbonates. It is so far the only system in the region where hydrothermal inputs have been well documented in terms of both facies and water chemistry [14,16]. The carbonate facies observed in Pastos Grandes are not restricted to the vicinity of hydrothermal springs, but can be found throughout the playa. Some of these facies have already been described, but their $\delta^{18}O$ and $\delta^{13}C$ signatures remain undocumented [12]. The aim of this study is to inventory the Laguna Pastos Grandes carbonate deposits, to measure their carbon and oxygen isotope compositions, and to interpret these results with regard to the parent waters. In addition to documenting the exceptional diversity of the carbonate fabrics found in this system, this study highlights the numerous environmental parameters to be considered for a correct interpretation of stable isotope signatures in ancient continental carbonate series, especially when several hydrological inputs (hypogean/meteoric) and the possible contribution of volcanic CO_2 may have played a role in carbonate mineralization.

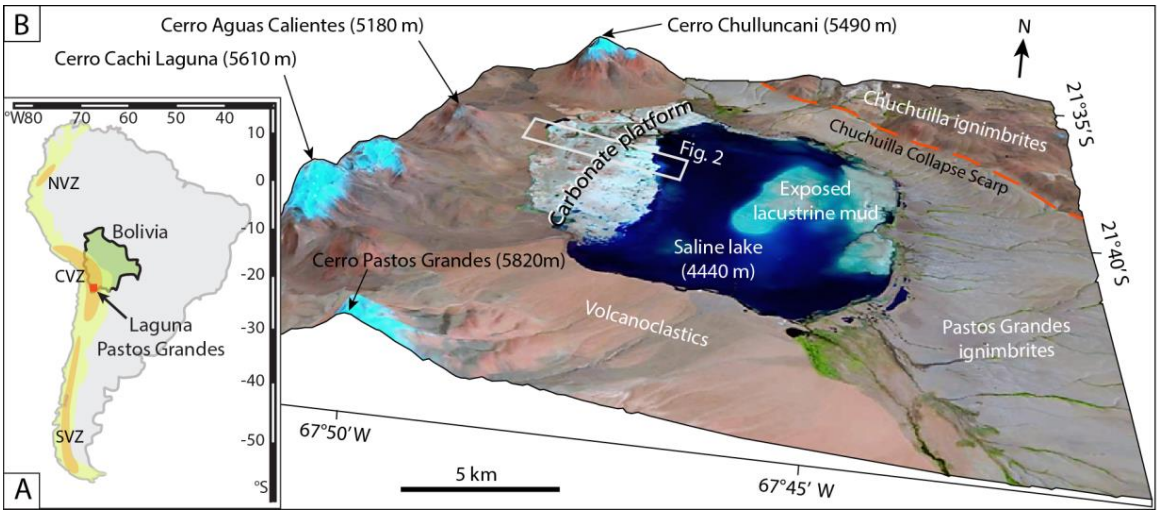

Figure 1. (**A**) General map of South America indicating Laguna Pastos Grandes located in the Central Volcanic Zone (CVZ). Yellow area: Andean Cordillera; NVZ = Northern Volcanic Zone; SVZ = Southern Volcanic Zone. (**B**) Sentinel-2 satellite image of the northern part of the Pastos Grandes Caldera Complex (Sentinel-2 satellite image of 18 February 2019, provided by Copernicus Open Access Hub, https://scihub.copernicus.eu/).

2. Regional Background, Volcanic Setting, and Carbonate Facies of the Pastos Grandes Area

The Andean Cordillera (South America) is a mountain range 7000 km long resulting from the subduction of the oceanic Nazca plate beneath the South American continental plate. This mountain range is also associated with a magmatic arc that spread all along the range. However, the distribution of this magmatism is heterogeneous due to the variation of the dip angle. Only locations above a high dip angle (~30°) present volcanic activity [17]. In the Central Andes, the volcanic activity is referred to as the Central Volcanic Zone (between 16° S and 28° S, Figure 1A), characterized by numerous andesitic volcanoes and calderas (e.g., [18]), and located at the west of the Altiplano and Puna Plateaus, large intermontane basins [19]. Additionally, these plateaus are separated by a large volcanic region, the Altiplano–Puna Volcanic Complex (APVC), covering 70,000 km^2 between 21° S and 24° S [20,21]. The APVC is formed by several calderas and stratovolcanoes, identified by approximately thirty ignimbrite deposits, composed of dacitic to rhyolitic rocks [21]. The activity of this volcanic complex spanned from 11 to 0.7 Ma [20–22], and its origin is thought to result from the steepening of the dip angle during the Late Miocene, favoring mantle melting and intense delamination of the lower continental crust [23,24]. This leads to the formation of a large magmatic body, the Altiplano–Puna Magmatic Body, identified by a 500,000 km^3 low-velocity zone between 4 and 25 km below sea level [25,26]. This magmatic body fed several shallower pre-eruptive chambers beneath the Altiplano–Puna Volcanic Complex [22,24].

The Laguna Pastos Grandes (−21.64° N; −67.79° E; 4450 m above sea level) is an extensive NW–SE elliptical playa (120 km^2) in the South Lipez region of Bolivia (Figure 1A). The laguna lies in the northeastern part of one of its calderas, the Pastos Grandes Caldera Complex [20], fed by one of the pre-eruptive chambers of the APVC, and shaped by two main eruptions: the Chuchuilla ignimbrite (5.45 ± 0.02 Ma) that ejected ~1200 km^3 of dense rock equivalent (DRE) of crystal-rich andesitic-to-dacitic rocks; the Pastos Grandes ignimbrite (2.89 ± 0.01 Ma) that ejected more than 1500 km^3 of DRE of crystal-rich dacites [21]. This eruption is thought to have resulted from a single, long-lived, monotonous intermediate magma flow, where near-eutectic conditions were maintained over ~1.1 Myr before and after the eruption by recurrent andesitic recharge, identified by chronochemical investigations [27]. This high-altitude area is characterized by a cold, dry climate [28]. Most precipitation occurs as summer rainfall, from December to March, with an annual mean of 100 mm/y, while dry conditions dominate during the rest of the year, with an evaporation rate of 1400 mm/y [29,30]. Air temperature can rise to +25 °C during the austral summer and fall to −30 °C during the austral winter [31].

The central and eastern parts of the playa are partly covered by an ephemeral shallow lake (maximum depth < 2 m) during the wet season, while the western part is a palustrine platform with hydrothermal springs and pools (Figure 1B). The ephemeral lake is fed by cool, fresh streams flowing from the Chuchuilla scarp on the eastern side, while the western and northern parts are characterized by piedmont springs, either cool and fresh, or warm and saline [14]. Lacustrine deposits are identified as mud containing gypsum, diatoms, volcanoclastics, and clay [10]. In the central part of the playa, the gypsiferous mud contains ulexite ore ($NaCaB_5O_9{\cdot}8H_2O$) [12].

The palustrine area is characterized by a carbonate-rich platform (approximately 40 km^2, up to 30 cm thick), fragmented by frost action [12], which is the largest carbonate platform in the Altiplano, where carbonate deposits are rare and restricted to smaller areas. As recently demonstrated, it results from hydrothermal fluids that deliver large quantities of CO_2 and Ca^{++} originating from the hydrothermal alteration of the volcanic basement in the presence of CO_2 [16]. Established models suggest that CO_2 comes exclusively from magmatism, deriving partly from the mantle (47%), indicating a deep origin for this gas. The recharge in chemical elements is thought to occur at 225 °C, based on geothermometers, corresponding to a depth of about 5 km [16], and may be triggered by the volcanic chamber under the laguna [22]. These hydrothermal fluids then rise to the surface through fractures [16]. The exceptional production of carbonates in this purely volcanic area could thus be explained by hypogean boosting of the sedimentary system. In fact, the CO_2 delivered by hydrothermal springs is from 60 to 389 mbar, equal to or higher than the amount at other Andean sites (see Reference [16]).

Previous sedimentary studies on Pastos Grandes have mainly documented diatom assemblages in submerged areas (e.g., [30]), and modern carbonates precipitated on some parts of the carbonate platform [12–14]. They report microbialites, rich in Ca and Si, which develop where moderately saline hot springs emerge, while pisolites (sub-spherical concretions up to 20 cm in diameter) form in small ponds farther from the springs. The other types of modern carbonate deposits occurring on the platform remain poorly described to date, both in terms of facies and geochemical characteristics.

3. Materials and Methods

Rock and water samples were collected during field investigations at Laguna Pastos Grandes in January 2016 (dry conditions) and March 2017 (wet conditions). Two sets of carbonate samples were distinguished: one from the vast, dried-up carbonate platform, and the second composed of present-day carbonates actively developing over the carbonate platform in ephemeral or perennial water conditions [12–14], associated with microbial mats that induce ongoing carbonate precipitation (see Reference [14]).

Carbonate deposits forming the carbonate platform were collected to constrain its approximate age of formation. Dating was carried out using U-series determination on six samples collected from the carbonate crust (n = 4), a pisolite core (n = 1), and calcitic mud (n = 1). They were analyzed at the GEOTOP research center, University of Quebec at Montreal, Canada (see details in Reference [32]). The calcite samples were cut using a diamond-abrading disc device (Dremel®rotary tool), and the external layers of the sample were removed to reduce the risk of contamination by ^{230}Th-bearing detrital particles. Each sample was dissolved with 7N HNO_3 in Teflon beakers, and a known amount of spike (^{233}U, ^{236}U, and ^{229}Th) was added to determine U and Th isotopes by the isotope dilution technique. The methods used for separation and purification of U and Th isotopes were based on Edwards et al. [33]. The purified U and Th fractions were dissolved in 2% HNO_3 and measured by MC-ICP-MS (multi-collector inductively coupled plasma mass spectrometry) with a NU II Instrument (Ametek, Berwyn, IL, USA). After mechanical cleaning, some detrital material was still present in the samples, as indicated by the low ^{230}Th/^{232}Th activity ratios (see Table 1). One of the main biases in U–Th dating is the presence of detrital elements. Correction for detrital contamination was performed following Ludwig and Paces [34], using an average crustal model (^{232}Th/^{238}U = 1.21 ± 0.65, ^{230}Th/^{238}U = 1 ± 0.1 and ^{234}U/^{238}U = 1 ± 0.1).

The sampled modern carbonates covering the carbonate platform (52 samples in total) include microbialites (n = 11), pisolites (n = 12), palmatoid concretions (n = 6), platystromatolites (n = 3), fusoid mud (n = 8), fusoid-bearing mud (n = 5), and anhedral mud (n = 7). Each facies is explained in detail in Section 4—Results (see also Table 2).

Microfacies were observed on polished slabs and polished thin sections. Thin sections were partially stained with alizarin Red-S to identify calcite, and potassium ferricyanide to identify ferrous carbonates. Thin sections were observed with a Nikon AZ100 microscope (Nikon, Tokyo, Japan) coupled with a Zeiss MrC5 camera (Carl Zeiss, Oberkochen, Germany). Scanning electron microscopy (SEM) was performed on soft sediments. Soft sediments were gold-coated and then observed with a Zeiss Auriga FEG-FIB microscope (Carl Zeiss, Oberkochen, Germany) at the IPGP (Institut de physique du globe de Paris, France) at an accelerating voltage of 15 kV, and a high current (up to 1 nA), to determine crystal morphology. Crystal chemical composition was determined with a Bruker Quanta 2000 EDX (energy-dispersive X-ray spectrometer; Bruker, Billerica, MA, USA) coupled to the microscope with the same voltage.

Whole rock mineralogy was determined by X-ray diffraction (XRD). Samples were crushed and flattened without orienting crystals. Whole rocks were analyzed at the Biogeosciences Laboratory (University of Burgundy, Dijon, France) with a Bruker D4 Endeavour diffractometer (Bruker, Billerica, MA, USA), with CuKα radiations, LynxEye detector, and Ni filter under 40 kV voltage and 25 mA intensity. Scanning from the goniometer ranged from 2° to 65° for each analysis.

Stable isotope analyses ($\delta^{18}O_{carb}$ and $\delta^{13}C_{carb}$) were performed at the Biogeosciences Laboratory (University of Burgundy, Dijon, France). Rock samples were cleaned with ethanol, and 30–50 µg of powder was retrieved from the most recent laminae using a Dremel drill with a diamond bit. Powder samples were dried at 50 °C for 12 h in a stove and then reacted with purified orthophosphoric acid at 70 °C in a ThermoFisher Kiel IV carbonate device connected to a ThermoFisher Delta V PLUS mass spectrometer (ThermoFisher Scientific, Waltham, MA, USA). The $\delta^{18}O_{carb}$ and $\delta^{13}C_{carb}$ values thus obtained were normalized to Vienna Pee Dee Belemnite (V-PDB), using international standard NBS-19 (see Table 3). Replicates were made to evaluate reproducibility at approximately 0.04‰ for $\delta^{13}C_{carb}$ and 0.08‰ for $\delta^{18}O_{carb}$, or better.

Measurements of the fraction modern carbon ($F^{14}C$) were obtained from the A.E. Lalonde Laboratory (Ottawa, ON, Canada) on 5 modern calcite samples (i.e., mushroom-like microbialite, shrub, pisolite, platystromatolite, and palmatoid), following the analytic protocol of St-Jean et al. [35]. The most recent laminae in these samples were abraded with a Dremel drill and diamond bit to remove impurities, and pre-etched with 0.2 N HCl to clean the outer surface. The cleaned samples were then completely dissolved in anhydrous H_3PO_4 and reacted overnight at room temperature. The CO_2 thus produced was extracted, cryogenically purified, and then converted into pure carbon by reacting with hydrogen and iron at 550 °C. The $^{12,13,14}C^{3+}$ ions were measured at 2.5 MV terminal voltage with Ar stripping, using a 3 MV tandem accelerator mass spectrometer (high voltage engineering). The fraction modern carbon $F^{14}C$ was calculated using the ratio of the sample $^{14}C/^{12}C$ ratio to the standard $^{14}C/^{12}C$ ratio (A.E. Lalonde Laboratory standard: Ox-II).

The carbon and oxygen isotope compositions of the carbonates ($\delta^{18}O_{carb}$, $\delta^{13}C_{carb}$, and ^{14}C) were acquired specifically for this study, while the data for water chemistry and stable isotopes ($\delta^{13}C_{gas}$, $\delta^{13}C_{DIC}$-dissolved inorganic carbon, and $\delta^{18}O_{water}$) from hydrothermal springs, piedmont sources, ephemeral streams, and the lake itself were taken from Muller et al. [16]. As no data were available for the depositional environments where the pisolites, palmatoid concretions, and platystromatolites formed, additional physicochemical measurements from the pools (i.e., temperature, pH, and conductivity) were acquired in situ with a Hach HQ40D Multi-instrument (Hach Company, Loveland, CO, USA). Water was also collected from several points and filtered in the field with a 1 µm filter. Filtrate composition was analyzed at the BRGM Laboratory (French Geological Survey, Orléans, France) and Total CSTJF Laboratory (Pau, France) laboratories using ion chromatography, atomic absorption spectrophotometry, inductively coupled plasma mass spectrometry (ICP-MS), colorimetry, the ion electrode method, and titration.

4. Results

4.1. Carbonates of Laguna Pastos Grandes and Dating

Laguna Pastos Grandes can be divided into two main domains with: (i) the upper and lower palustrine carbonate platforms covered by hydrothermal springs and pools [14]; (ii) a shallow, ephemeral saline lake (Figure 2A; Figure S1). The carbonates of the first domain corresponding to the palustrine platforms, and associated carbonates currently forming over it in springs and pools were dated by the U–Th and ^{14}C methods, respectively.

The U–Th method was used to determine the average age of the carbonate platform (Table 1; Supplementary Materials, Table S1). The ages obtained on the upper platform came from a carbonate crust composed of an assemblage of cemented calcitic grainy facies, with pisolites, intraclasts, peloids, and ooids (Figure 3A) [14]. They ranged from 1 ka (kiloannum) to 2 ka, indicating the recent development of this platform. The lower platform was mostly formed of white calcite mud (Figure 2C), with pluricentimetric calcitic clasts (resulting from active cryoturbation; Figure 2C). The range of ages obtained from the clasts and muds was much greater than for the upper carbonate platform: botryoidal cement clast (Figure 3B) approximately 3.5 ka; peloidal grainstone clast approximately 34 ka, and mud approximately 13 ka. Nevertheless, the mud was sampled in a reworked location (cryoturbation),

probably removing several underlying layers, which would prevent precise dating. The clast composed of peloidal grainstone was found in the southern area where the alluvial fan intrudes into the carbonate platform. This region is characterized by a major influx of volcanoclastics mixing and reworking carbonates, which could come from lower layers of the palustrine area (Figure 2D). Overall, the stability of the facies preserved on the upper platform made the ages obtained more robust, and a Holocene estimation was therefore proposed for the deposition of the platform. Nevertheless, a greater number of ages would be useful to ensure that the variability of ages recorded did not result from a re-opening of the carbonate system [36].

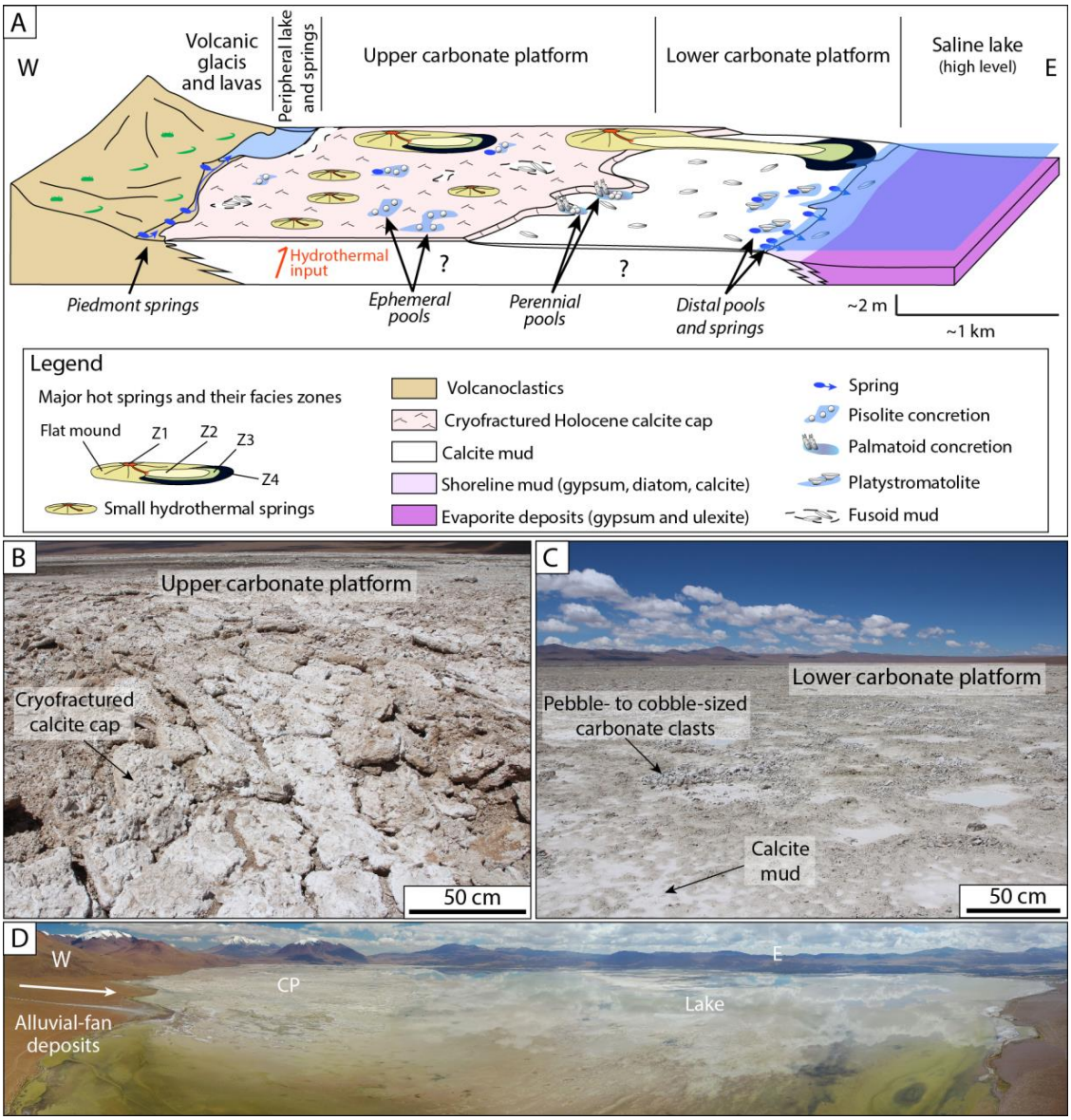

Figure 2. (**A**) Depositional environments in the western part of Laguna Pastos Grandes (see Figure 1A). Zone 1 to Zone 4 (Z1–Z4) are depositional zones associated with the main hydrothermal springs, described in Bougeault et al. [14]: Z1, the hydrothermal feeding system; Z2, the apron; Z3, the proximal–distal transitional belt; Z4, the distal zone. (**B**) Field view of the Holocene calcite cap fragmented into pluridecimetric slabs, upper carbonate platform. (**C**) Field view of the mud-dominated surface of the lower carbonate platform with cryoclasts from the recent calcite cap. (**D**) Panoramic drone view of Laguna Pastos Grandes, showing the southern part of the carbonate platform (CP) and the shallow lake covering most of the playa during a wet period (March 2017).

Table 1. The U–Th ages (before 2020) from the carbonate platform. All U–Th ratios are activity ratios. uncorr. = uncorrected; corr. = corrected

Sample	Sample type	Position	^{238}U (ppb)	^{232}Th (ppb)	^{234}U/^{238}U	^{230}Th/^{234}U	^{230}Th/^{238}U	^{232}Th/^{238}U	^{230}Th/^{232}Th	^{230}Th/U Age ka (uncorr.)	^{234}U/^{238}U$_{init.}$	^{230}Th/U Age ka (corr.)	^{234}U/^{238}U$_{init.}$
PG17-14	Pisolite core	Upper Platform	309.488 ± 0.943	59.141 ± 0.18	1.570 ± 0.006	0.043 ± 0.0001	0.067 ± 0.0002	0.063 ± 0.0003	1.068 ± 0.0057	4.714 ± 0.024	1.578 ± 0.0056	1.085 ± 2.009	1.603 ± 0.0197
PG17-33	Pisoidic rudstone	Upper Platform	690.160 ± 4.21	33.395 ± 0.153	1.528 ± 0.012	0.018 ± 0.0003	0.027 ± 0.0004	0.016 ± 0.0001	1.729 ± 0.0270	1.964 ± 0.034	1.531 ± 0.0121	1.031 ± 0.511	1.537 ± 0.0129
			660.145 ± 4.458	27.480 ± 0.242	1.530 ± 0.013	0.016 ± 0.0003	0.024 ± 0.0005	0.014 ± 0.0002	1.775 ± 0.0353	1.73 ± 0.036	1.533 ± 0.0129	0.929 ± 0.439	1.538 ± 0.0135
PG17-37	Peloidal grainstone	Upper Platform	207.194 ± 0.787	9.175 ± 0.04	1.537 ± 0.011	0.026 ± 0.0006	0.040 ± 0.0009	0.014 ± 0.0001	2.726 ± 0.062	2.828 ± 0.066	1.541 ± 0.0106	1.979 ± 0.466	1.547 ± 0.0113
			220.421 ± 1.742	12.517 ± 0.065	1.523 ± 0.014	0.027 ± 0.0004	0.041 ± 0.0007	0.019 ± 0.0002	2.211 ± 0.0336	2.968 ± 0.055	1.528 ± 0.0137	1.869 ± 0.601	1.534 ± 0.0147
PG17-63	Peloidal grainstone	Lower Platform	183.093 ± 0.743	1.926 ± 0.021	1.295 ± 0.007	0.276 ± 0.0022	0.357 ± 0.0028	0.003 ± 0.00004	103.752 ± 1.4111	34.626 ± 0.379	1.328 ± 0.0071	34.393 ± 0.396	1.326 ± 0.0071
			185.364 ± 0.763	1.589 ± 0.01	1.286 ± 0.009	0.271 ± 0.0023	0.348 ± 0.0027	0.003 ± 0.00002	124.076 ± 1.1664	33.899 ± 0.412	1.315 ± 0.0093	33.707 ± 0.423	1.316 ± 0.0093
PG17-69	Botryoidal cement	Lower Platform	56.647 ± 0.22	3.412 ± 0.024	1.561 ± 0.011	0.042 ± 0.0012	0.065 ± 0.0018	0.020 ± 0.0002	3.323 ± 0.0967	4.649 ± 0.138	1.568 ± 0.0111	3.513 ± 0.629	1.576 ± 0.0125
			52.889 ± 0.205	1.646 ± 0.007	1.547 ± 0.008	0.029 ± 0.0005	0.045 ± 0.0007	0.010 ± 0.0001	4.402 ± 0.0736	3.191 ± 0.056	1.552 ± 0.0081	2.600 ± 0.326	1.556 ± 0.0086
PG17-77	Fusoid mud	Lower Platform	175.713 ± 0.909	131.034 ± 0.721	1.589 ± 0.011	0.231 ± 0.0019	0.368 ± 0.003	0.244 ± 0.0018	1.507 ± 0.0137	28.148 ± 0.349	1.638 ± 0.0119	13.737 ± 7.765	1.767 ± 0.1078

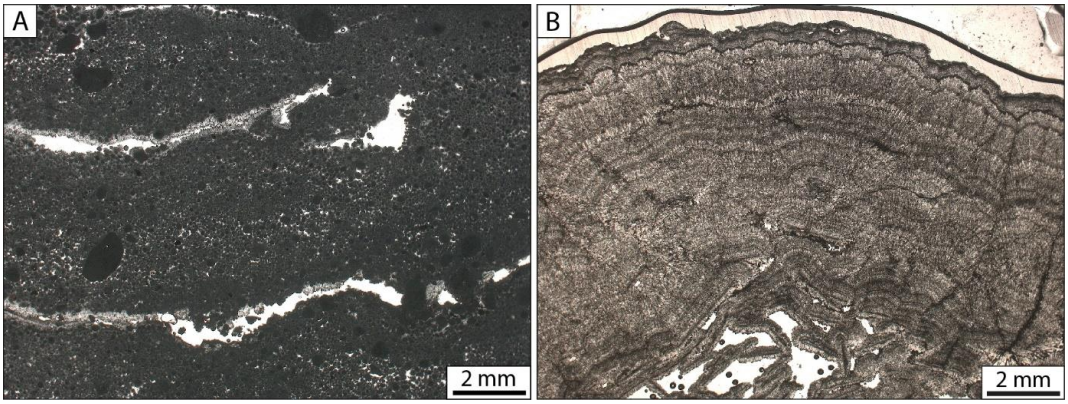

Figure 3. Example of two facies of the carbonate platform dated by U–Th: (**A**) a grainstone composed of calcitic peloids (10–200 µm), showing elongated cavities partly filled by dog-tooth sparite (PG17-37, ~2.0 ka) and (**B**) a botryoidal calcitic crust (PG17-69, ~3.0 ka).

The Holocene deposits of the upper carbonate platform are locally covered by hydrothermal springs, discharging hot acidic waters, but also ephemeral pools filled during the wet season, triggered by a water-table rise. Several large perennial "mid-platform pools" have formed just below the edge of the upper platform, which is approximately 30 cm higher than the lower platform (Figure 2A; Figure S1). The limit between the lower platform and the ephemeral central lake (Figure 2D) fluctuates due to water-level variation, coinciding with numerous "distal springs" caused by hydrothermal seepage. Observations and quantitative analyses of the area covered by the lake based on satellite views (2000–2019) show that the central lake evaporates almost completely every year (Figure S2), triggering gypsum and ulexite sedimentation in the playa [10]. Here, in contrast with the methods used for the carbonate platform, the age of these modern carbonate deposits associated with hydrothermal springs and pools was obtained using ^{14}C dating (see Section 4.3). The facies corresponding to the hydrothermal springs have been described in Reference [14], and the ones from pools are described below (Section 4.2.).

4.2. Modern Calcite Facies and Parent Waters

Above recent facies of the carbonate platform, five groups of facies (including one or more sub-facies) and their associated parent waters were identified along a W–E transect from the volcanic glacis to the lake (Figure 2A).

4.2.1. Microbialites

Microbialites develop in association with hydrothermal springs, mainly found in the northern part of the upper platform (Figure S1). Hydrothermal springs emerge at the top of large flat mounds, composed of brownish-to-reddish sediments containing diatoms, calcite mud, calcite intraclasts, and iron oxide [14]. Waters at the vents are hot (20 to 75 °C) and slightly acidic (pH ~5.8–6.9) [12,16]. They are moderately saline (10–17 mg·L^{-1}; electrical conductivity: 19–30 mS·cm^{-1}), and enriched in Na and Cl ions with K, Mg, Li, Ca, and Si. The main gas emitted was CO_2 with an elevated partial pressure reaching 309 mbar. Expelled fluids fed successive depositional zones, upstream to downstream: a central pool, a channel, an apron, a proximal–distal transitional belt, and a distal zone (Figure 4A). In this distal zone, hydrothermal waters evaporate or sink beneath the Holocene carbonate cap, feeding the underlying water table.

Along the hydrothermal pathway, several microbialite morphologies were observed: ledge, mushroom-like, cerebroid, snake-like, isolated shrub, and planar shrub structures (Figure 4B–D; Table 2). These microbialites were mainly composed of micritic laminae, bundles of microbial sheaths, diatom accumulations, and/or silica laminae. (Further details of macro- to microscale microbialite analyses and associated depositional environments can be found in Bougeault et al. [14]).

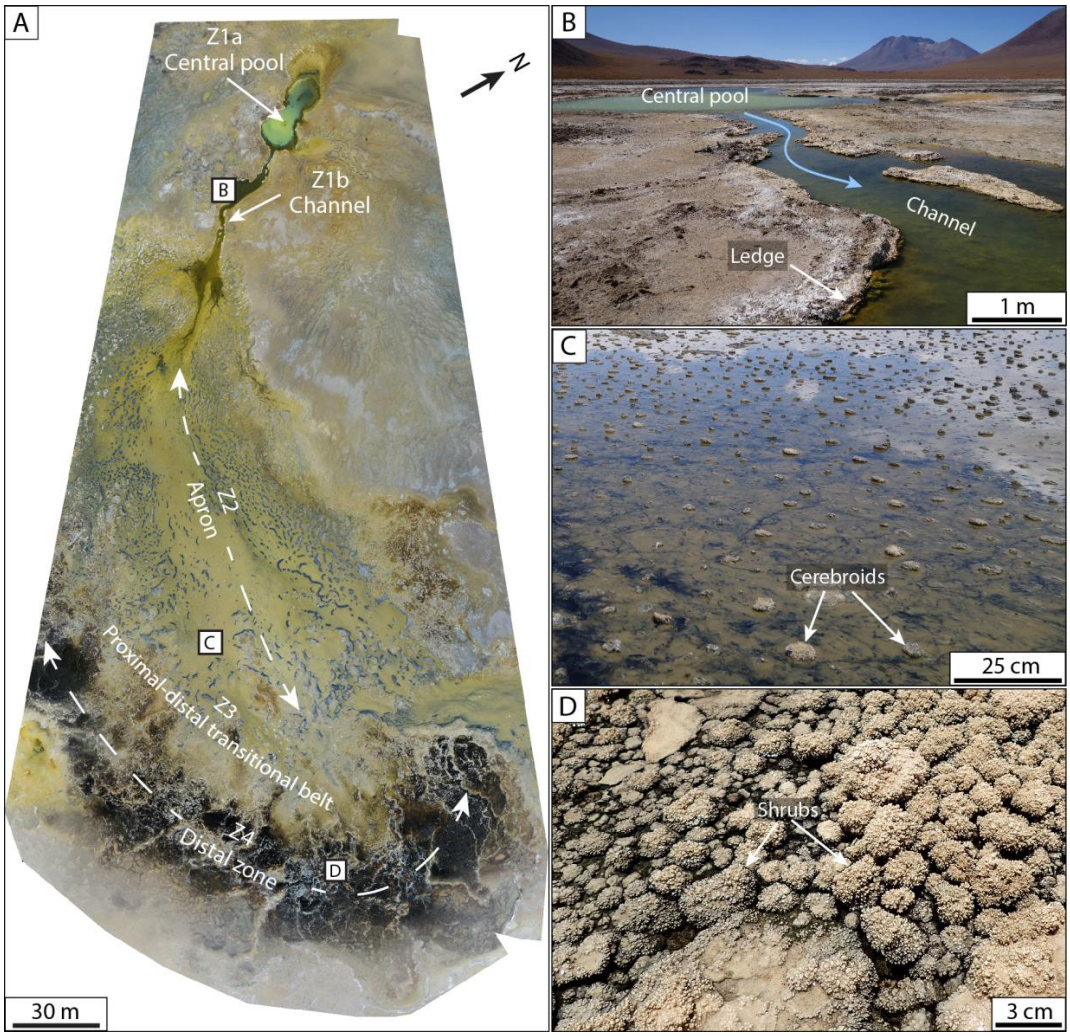

Figure 4. La Salsa hydrothermal system (see Figure S1) and associated facies [14]: (**A**) air drone image of the hydrothermal discharge of La Salsa, showing depositional zones (Z1–Z4); (**B**) outflow channel (Z1a–Z1b) with well-developed ledge microbialites. Dense microbial mats cover the channel floor; (**C**) apron (Z2), with numerous cerebroid microbialites, developing on mud composed of diatoms and aggregated anhedral calcite crystals; (**D**) calcite shrubs in association with black microbial mats in the distal zone (Z4).

Table 2. Description of modern facies and associated depositional environments, based on macro-, meso-, and microscopic structures. Physicochemical parameters of all depositional environments were measured during field investigations in January 2016 and March 2017. UCP and LCP refer to upper and lower carbonate platforms.

Facies	Macro to Mesostructures		Microstructures	Depositional Environments		Diurnal Physicochemical Parameters (January 2016 and March 2017)
		Size				
Ledge microbialite	Planar laminated microbialite; lateral development in terraces	2 to 5 cm thick; 5–20 cm long	Alternating laminae composed of micrite, filament-rich bundles, and diatoms; the upper and lateral parts of the structures (ledge and mushroom-like) show a transition from filament-rich bundles to micrite; sheltered parts are infilled by micrite with diatoms and ostracods; bundles composed of casts and molds of filaments	Main hydrothermal springs located on the UCP (La Salsa spring, see Bougeault et al. [14]	Z1—Central pool and outflow channel	T: 42 to 36 °C pH: 5.8 to 7.2 σ: 25–27 mS·cm^{-1}
Mushroom-like microbialite	Dome-shaped structure developing on intraclasts; planar to laterally curved laminae	5 to 10 cm in diameter				
Cerebroid microbialite	Irregular ovoid structure; organized in planar and columnar laminae	2 to 20 cm in diameter			Z2—Apron	T: 38 to 21 °C pH: 7.1 to 8.2 σ: 26–55 mS·cm^{-1}
Snake-like structure	Hemispherical and tortuous structure with white crust on upper part; white crusts locally covered by mm micrite and silica-rich branches; organized in laminae and clots	10 cm to 1 m long	Alternation of densely and loosely packed peloid-rich laminae with diatoms, top structure showing siliceous cements and gypsum between grains		Z3—Proximal–Distal Transitional belt	T: 25 to 21 °C pH: 8 to 8.8 σ: 32–68 mS·cm^{-1}
Isolated shrub	Dome-shaped structure covered by millimetric branches; planar to columnar laminae	2 to 5 cm in diameter	Alternation of micritic, spiritic, and siliceous laminae, coating extraclasts (carbonate pebbles, spherulites, pisolites, detrital grains); millimetric branches (microstromatolites) are composed of micrite and silica		Z4—Distal zone	T: 21 to 20 °C pH: 7.7 to 6.9 σ: 48–225 mS·cm^{-1}
Planar shrub	Shrub with millimetric branches organized as a ring around a planar central area; planar to columnar laminae	Ranging from 5 to 50 cm				
Pisolite concretion	Ovoid to spherical concretion; concentric laminae	Few mm to 20 cm in diameter	Alternating micritic, sparitic, and amorphous silica laminae around spherulites, carbonate or detrital grains	Ephemeral to perennial pools on the UCP and the UCP-LCP transition		T: 18.5–21 °C pH: 7.3–7.8 σ: 38.8–73 mS·cm^{-1}
Palmatoid concretion	Horizontally spreading or columnar structure with branches at the top	5 to 15 cm long	Micritic, sparitic, and amorphous silica laminae passing into a bud-like shape at the top of the concretion	Perennial pools at the transition between UCP and LCP		T: 18 °C pH: 7.8 σ: 62 mS·cm^{-1}
Platystromatolite	Plate-shaped structure; wrinkled to columnar laminae	From 5 to 25 cm in diameter	Mainly planar to wavy micritic, with rare sparitic and Fe-oxide layers, growing over and around an extraclast (carbonate pebbles, pisolites)	Distal pools and springs on the LCP and at the transition between the LCP and the ephemeral lake		T: 23°C pH: 7.5 σ: 69–127 mS·cm^{-1}
Anhedral calcite mud	Mud; structureless, disturbed by bioturbation (flamingos)	-	Anhedral crystals of calcite, associated with diatoms, forming aggregates	Produced in water discharge of hydrothermal springs		T: 42 to 21 °C pH: 5.8 to 8 σ: 25–68 mS·cm^{-1}
Fusoid mud	Mud; structureless, disrupted by cryoturbation	-	Elongated scalenohedral crystals of calcite (5 to 100 m long, with curved faces and edges resulting in a fusoid shape. Associated with rare diatom frustules and halite crystals	Ephemeral shallow puddles covering the LCP and, to a lesser extent, the UCP		T: 15–24 °C pH: 7.4–8 σ: 48 mS·cm^{-1} to saturation
Fusoid-bearing mud	Accumulation of beige to brown mud; structureless	-	Mud containing silt- to clay-sized particles with variable proportions of fusoid calcite crystals (5–20%), detrital grains (quartz, feldspar), gypsum, halite, and rare diatoms	Ephemeral central lake; during highstand lake level		T: 15–24 °C pH: 7.4–7.65 σ: 179 mS·cm^{-1} to saturation

4.2.2. Pisolites

Pisolites are non-fixed, spherical-to-ovoid carbonate concretions from a few millimeters to 20 cm in diameter, found in ephemeral or perennial pools (Figures 2A and 5A). Rainfall during the wet season triggers a rise in the water table, filling depressions in the upper carbonate platform, thus forming shallow ephemeral pools (<20 cm deep). Some pools are associated with hydrothermal seepage through the fractured carbonate cap, associated with iron oxide precipitation (Figure 5B). At the transition between the upper and lower platforms, deeper perennial pools (<50 cm deep) are fed by the water table (Table 2). In these perennial pools, pisolites are often cemented to the floor, commonly fusing together to form large slabs (20–30 cm thick) which can cover several square meters (Figure 5C). Physicochemical parameters for both ephemeral and perennial pools recorded during the wet season indicate pH values between 7.3 and 7.8, and electrical conductivity between 39 and 73 mS·cm^{-1}. The water isotope composition measured at one of these pools during the wet season (March 2017) was 4.87‰ for $\delta^{13}C_{DIC}$ and −3.4‰ for $\delta^{18}O_{H2O}$. Great seasonal variation is nevertheless to be expected.

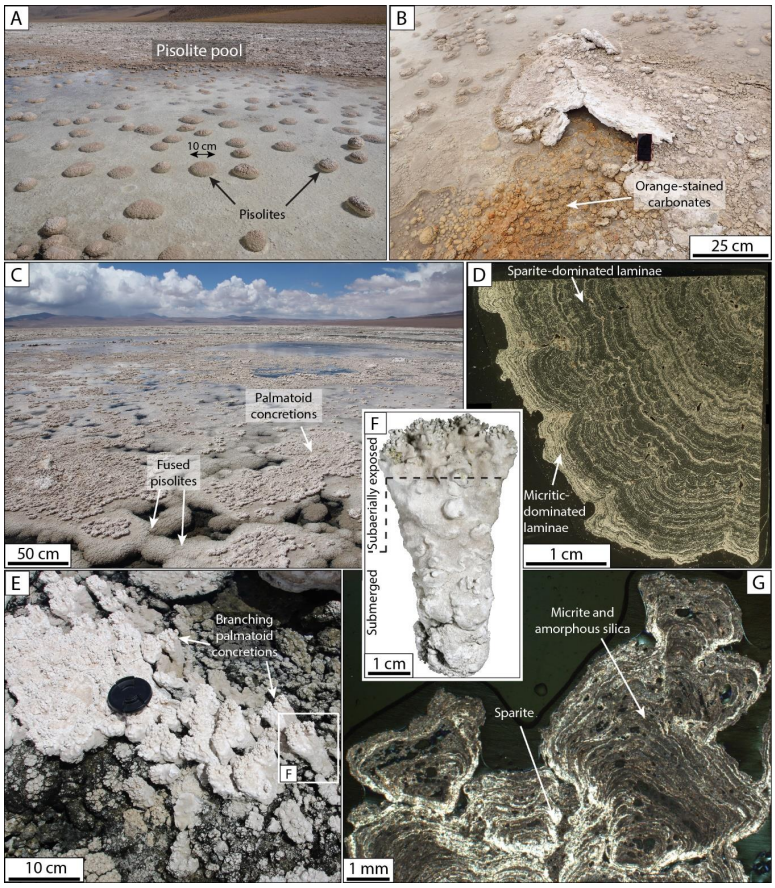

Figure 5. Calcite concretions in ephemeral and perennial pools: (**A**) a shallow pool on the upper platform, with large pisolites, observed at the start of the wet season; (**B**) an example of fracture-related seepage into a pisolite pool. Water from the carbonate platform is accompanied by Fe-oxide precipitation, resulting in orange-stained carbonates; (**C**) a perennial pool showing coalescent pisolites forming large slabs covered by branching palmatoid concretions; (**D**) reflected light view of a pisolite (thin section) showing alternating micrite (white laminae) and sparite (grey laminae); (**E**) columnar palmatoid concretions growing from the floor in a perennial pool; (**F**) close-up view of (**E**), showing the lower (submerged) and upper (subaerially exposed) parts of a columnar palmatoid concretion; (**G**) cross-polarized light view of shrub-like branches at the top of a columnar palmatoid concretion. Micritic and amorphous silica laminae (grey to brown) alternate with sparitic laminae (white). Sparite preferentially develops under shrub-like branches.

At the microscale, pisolites are composed of alternations of sparitic, micritic, and amorphous silica laminae (Figure 5D), often developing around a nucleus (e.g., calcite clast or volcanic mineral) (Table 1). Their concentric spherical form probably results from freeze/thaw processes [11,12] but also from wind action [11], which could occasionally trigger displacements, thus grouping small pisolites into symmetric ripples, for example.

4.2.3. Palmatoid Concretions

Palmatoid concretions are fixed concretions developing in perennial pools, at the upper–lower platform transition (Figure 2A, Table 2). These "arborescent" concretions were first mentioned by Risacher and Eugster [12]. Here, they are called palmatoid concretions, because they are similar in appearance to *Acropora palmata* corals. Some grow from pool floors, forming ~10 cm columnar concretions, divided into a submerged part (Figure 5E,F), composed of continuous laminae with regular alternations of micrite and sparite, and an aerially exposed part at the air–water interface (Figure 5E–G), composed of millimetric branches with discontinuous laminae of micrite, sparite, and amorphous silica. These aerial branching structures can also form on top of pisolites, growing horizontally rather than vertically (Figure 5C,G). During windy conditions, considerable water oscillation and spray affect the upper part of palmatoid concretions [12].

4.2.4. Platystromatolites

Platystromatolites are stromatolites with a plate-shaped morphology, developing in the distal part of the lower carbonate platform, in very shallow "distal" pools (<10 cm deep), surrounded by soft sediment (Figure 6A,B). They are frequently associated with small springs (seepages), indicated by a brown-to-reddish color due to Fe-oxide impregnation in the surrounding sediments. This area can be temporarily flooded by the saline lake during the wet season. Physicochemical parameters measured in March 2017 indicated a pH of 7.5 and electrical conductivity of 70 mS·cm^{-1}, rising to 127 mS·cm^{-1} for pools close to the lake.

Thin sections of these structures show that they start to grow on rock fragments (mostly calcite clasts) in the mud and gradually acquire their plate-shape at the air–water interface, like micro-atolls. They are composed of successive micritic laminae, incorporating detrital grains and microbial filaments (Figure 6C, Table 2).

4.2.5. Calcite Mud

Mud containing calcite crystals covers large areas at Laguna Pastos Grandes. Two main types of mud can be identified, based on depositional setting, micro-texture, and elemental composition (Table 2).

The first type, anhedral mud, is composed of small anhedral crystals of calcite a few µm in size, formed in proximal-to-intermediate depositional zones of hydrothermal systems (Z1–Z2, see Figure 4A–C), as observed by Bougeault et al. [14]. Anhedral mud is often associated with diatom frustules, forming micritic aggregates (Figure 5D).

The second type, fusoid mud, is composed of fusoid crystals of calcite, approximately 3 to 100 µm in length along the *c*-axis, with a length-to-width ratio of 4 to 5. Fusoid calcite crystals exhibit a scalenohedral morphology, with faces delimited by curved edges (Figure 6E,F). The XRD analysis identifies this calcite as a low magnesian calcite (main diffraction peak d_{001} at 3.03 Å) but EDX analysis indicates a non-negligible percentage of magnesium (~3.4 mol% $MgCO_3$), reaching the range of intermediate magnesium calcite noted by Rucker and Carver [37]. Similar morphologies have been observed in several Chilean lakes, determined as ikaite or calcite pseudomorphs after ikaite (e.g., Laguna Lejía [38]; Laguna Potrok Aike [39]; Laguna Cháltel [40]).

Fusoid mud precipitates in many places, but not in the purely hydrothermal systems, and can be divided into two subgroups based on calcite crystal content. The first subgroup, containing 90% to 95% of calcite, was observed in both the upper and lower platforms. In the upper platform, fusoid calcite mud can be observed in pools, occasionally associated with pisolites. In the lower platform, fusoid mud

was more frequent, and was characterized by thin whitish deposits, mostly in very shallow depressions (See Figure 2C). The second type, containing less than 20% of fusoid calcite, was termed fusoid-bearing mud. It was found in the eastern part of the playa, covered by the ephemeral lake, and associated with gypsum, volcanoclastic grains, and diatoms (Figure 6G).

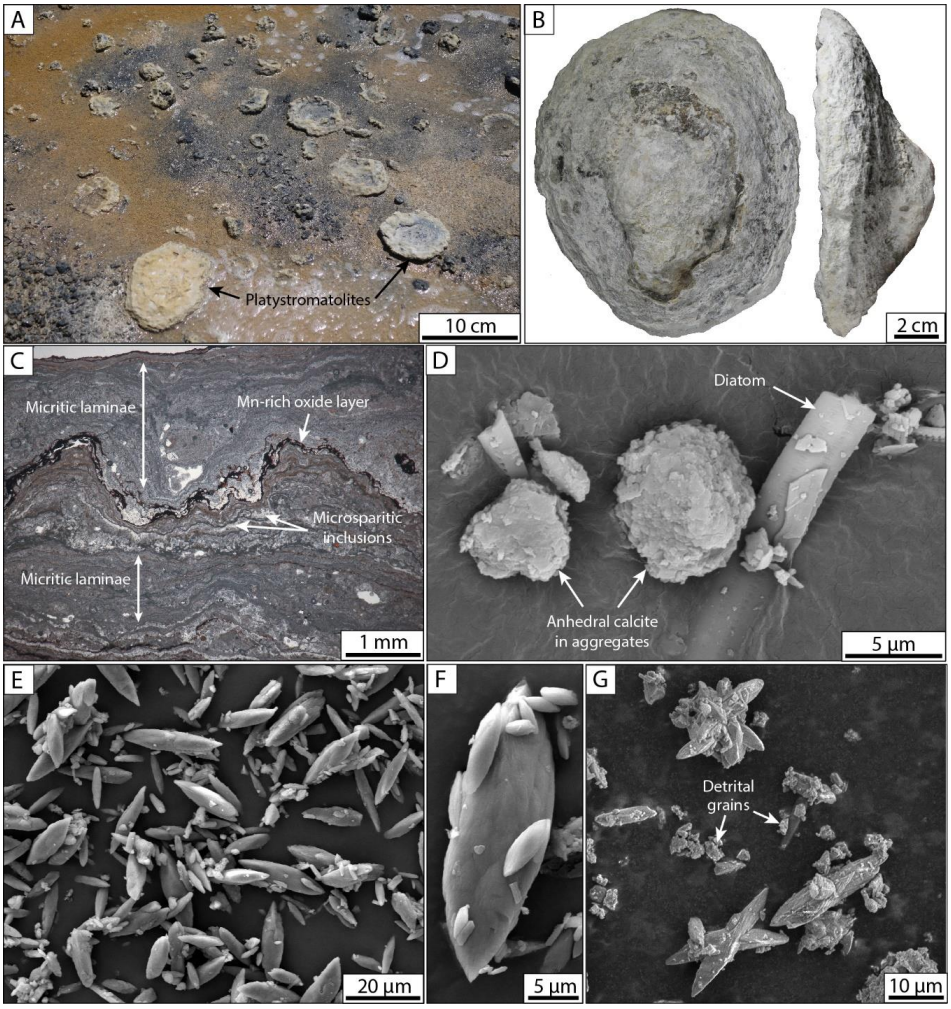

Figure 6. Platystromatolites and mud deposits: (**A**) field view of platystromatolites precipitating in a very shallow pool on the lower platform. Mud surrounding platystromatolites is brown to reddish in color due to the seepage near the pool transporting iron; (**B**) top and lateral view of a platystromatolite; (**C**) plane polarized light view of laminae from the top of a platystromatolite. They are mainly composed of planar-to-wavy micritic laminae, with local microsparitic inclusions. Corrosion surfaces are well identified by Mn-oxide layers; (**D**) SEM view of aggregates containing anhedral calcite crystals and diatom fragments, La Salsa hydrothermal spring (working distance of 13 mm and using backscattered electron detector); (**E**) SEM view of a fusoid mud composed of fusoid crystals of calcite from the lower platform (working distance of 8.6 mm and using secondary electron detector, also for (**F**) and (**G**)); (**F**) Zoom-in view of a fusoid calcite crystal showing curved faces and edges; (**G**) SEM view of a fusoid-bearing mud from the ephemeral central lake, showing fusoid calcite crystals and very small detrital particles.

4.3. Isotope Geochemistry of Modern Carbonates

4.3.1. Carbon and Oxygen Stable Isotopes

A broad range of low-to-high $\delta^{13}C_{carb}$ and $\delta^{18}O_{carb}$ values was recorded in these modern carbonate facies, along a transect from the western margin to the lake, exclusively composed of calcite (Figure 7A; Table 3). Calcite from microbialites in the hydrothermal La Salsa system showed the

greatest amplitude, with values ranging from −1.4‰ to +10.8‰ for $\delta^{13}C_{carb}$, and −12.6‰ to −2.0‰ for $\delta^{18}O_{carb}$, with the lowest value recorded in the central pool, and the highest in the distal zone (Figure 7A). Downstream along the transect (Figure 7B), three trends were observed for $\delta^{13}C_{carb}$: (1) a moderate increase in Z1 (−1.4‰ to +4.0‰); (2) a relative stability from Z2 to Z3 (+4.0‰ to +3.1‰); and (3) a stronger increase in Z4 (+3.1‰ to +10.8‰). For $\delta^{18}O_{carb}$ values, three trends were also distinguished: (1) an increase from Z1 to Z2 (−11.5‰ to −6.6‰); (2) a relative stability in Z2; −6.6‰ to −7.3‰); and (3) a further increase from Z3 to Z4 (−7.3‰ to −2.0‰).

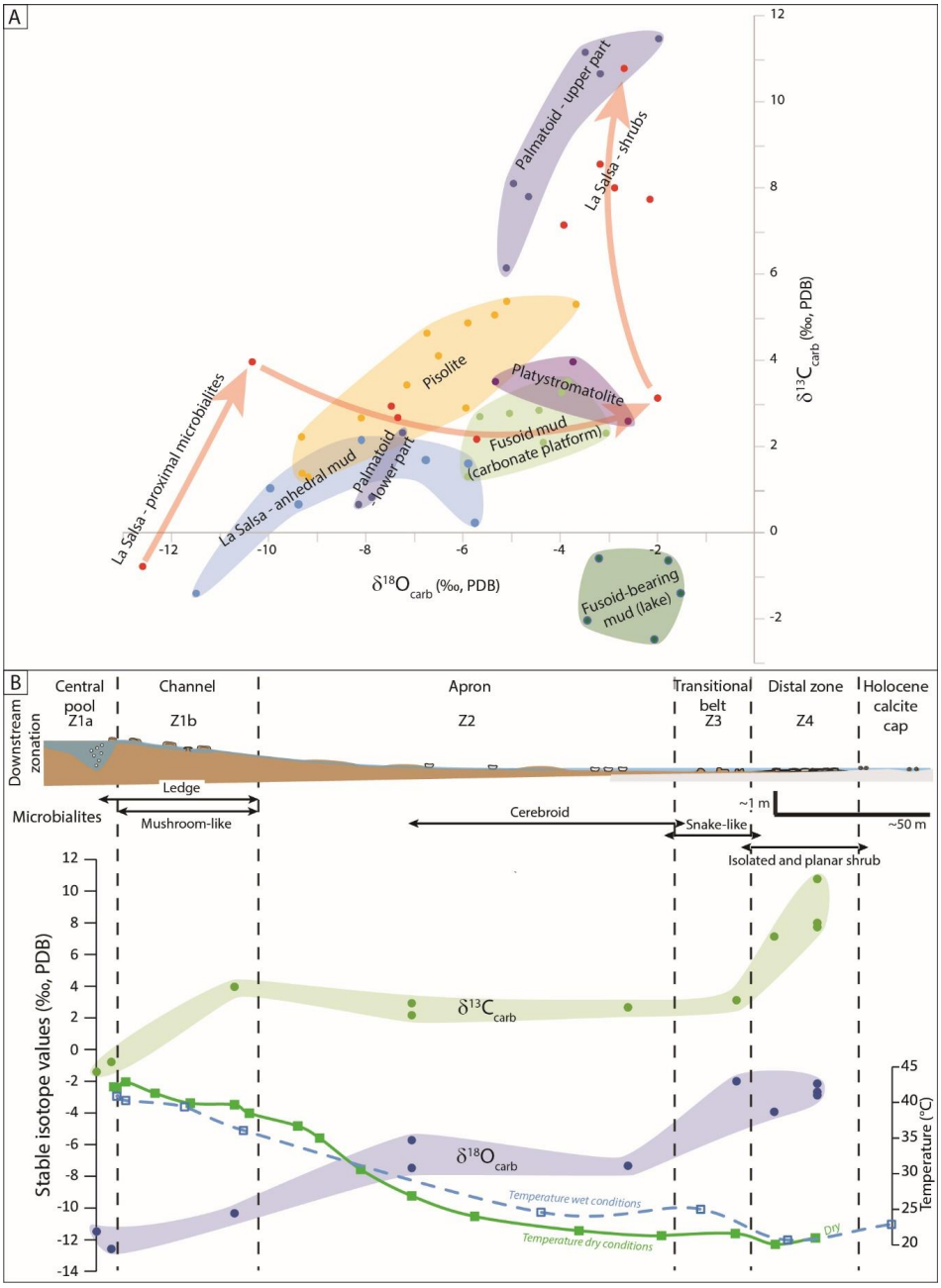

Figure 7. (**A**) Carbon and oxygen isotope composition of the calcitic facies of Laguna Pastos Grandes. (**B**) Downstream evolution of carbon and oxygen isotopes in calcite-rich microbialites along the hydrothermal La Salsa pathway. Water temperatures were taken from Bougeault et al. [14].

Table 3. Carbon and oxygen isotope composition, with some ^{14}C dating of modern facies observed in Pastos Grandes, along a transect from the western margin to the lake. UP = upper carbonate platform; UPT = upper-lower platform transition; LP = lower carbonate platform; L = lake.

Facies			Sample	Position	Latitude (°N)	Longitude (°E)	$\delta^{13}C$	$\delta^{18}O$	$F^{14}C$	^{14}C Age (yr BP) *
Pisolite concretion			PG17-9	UP	−21.62077	−67.8499	2.66	−8.09	0.0639	22,088 (±70) *
			PG17-14	UP	−21.62077	−67.8499	2.22	−9.32		
			PG17-12	UP	−21.62077	−67.8499	3.43	−7.15		
			PG2-7	UP	−21.61994	−67.85074	2.89	−5.94		
			PG2-21	UP	−21.61961	−67.85279	5.05	−5.35		
			PG2-6	UP	−21.61976	−67.85204	5.37	−5.10		
			PG17-54	UP	−21.59494	−67.82934	1.29	−9.19		
			PG17-52	UP	−21.59301	−67.8309	1.38	−9.31		
			PG17-80	UP	−21.61983	−67.84538	4.63	−6.74		
Fusoid mud			PG17-38	UP	−21.64951	−67.83747	3.26	−3.96		
			PG17-30	UP	−21.65398	−67.84463	2.31	−3.05		
			PG17-34	UP	−21.65156	−67.8411	2.77	−5.04		
			PG17-57	UP	−21.59722	−67.82633	2.84	−4.43		
			PG17-59	UP	−21.5997	−67.82579	2.69	−5.65		
Microbialites—La Salsa	Z1	Ledge	PG1−2	UP	−21.61934	−67.84836	−0.79	−12.59		
		Mushroom	PG1−6	UP	−21.61951	−67.84805	3.96	−10.33	0.0469	24,577 (±94) *
	Z2	Cerebroid	PG1−11	UP	−21.61987	−67.84746	2.93	−7.47		
			PG1−14_1	UP	−21.61929	−67.84652	2.17	−5.72		
			PG1−14_2	UP	−21.61929	−67.84652	2.67	−7.34		
	Z3	Snake-like	PG2−45	UP	−21.61955	−67.84622	3.12	−1.99		
	Z4	Shrub	PG1−17	UP	−21.61947	−67.84598	7.14	−3.92		
			PG1−18_1	UP			7.74	−2.15		
			PG1−18_3	UP	−21.61962	−67.84782	8.00	−2.88		
			PG1−18_4	UP			10.77	−2.68	0.1068	17,965 (±63) *
			PG17−16	UP	−21.61957	−67.8458	8.55	−3.18		
Mud—La Salsa	Z1	Anhedral mud	PG1−S	UP	−21.61932	−67.84841	−1.41	−11.49		
			PG1−5	UP	−21.61955	−67.84817	0.65	−9.38		
	Z2	Anhedral mud	PG1−8	UP	−21.61962	−67.84782	0.22	−5.76		
			PG1−10	UP	−21.61974	−67.84759	1.61	−5.89		
			PG1−11bis	UP	−21.61987	−67.84746	1.03	−9.96		
			PG1−12	UP	−21.61978	−67.84722	1.69	−6.77		
			PG1−13	UP	−21.61955	−67.84689	2.15	−8.09		
Pisolite			PG17-46a	ULT	−21.64688	−67.83166	4.87	−5.90		
			PG17-46b	ULT	−21.64688	−67.83166	4.10	−6.50		
			PG17-46c		−21.64688	−67.83166	5.30	−3.67		

Table 3. *Cont.*

Facies	Sample	Position	Latitude (°N)	Longitude (°E)	$\delta^{13}C$	$\delta^{18}O$	$F^{14}C$	^{14}C Age (yr BP) *
Palmatoid concretion	PG17-43a_top	ULT	−21.64674	−67.83198	8.10	−4.96	0.0333	27,327 (± 96) *
	PG17-43b_top	ULT	−21.64674	−67.83198	7.80	−4.65		
	PG17-43d_top	ULT	−21.64674	−67.83198	6.14	−5.11		
	PG17-43d_bot	ULT	−21.64674	−67.83198	0.65	−8.15		
	PG17-43c_top	ULT	−21.64674	−67.83198	11.15	−3.48		
	PG17-43c_bot	ULT	−21.64674	−67.83198	0.82	−7.88		
	PG17-43e_top	ULT	−21.64674	−67.83198	10.65	−3.17		
	PG17-43e_bot	ULT	−21.64674	−67.83198	2.32	−7.24		
	PG17-48b	ULT	−21.64688	−67.83166	11.46	−1.97		
Fusoid mud	PG17-44	ULT	−21.64666	−67.83168	3.51	−3.84		
Fusoid mud	PG17-65c	LP	−21.66899	−67.81787	1.30	−5.90		
	PG17-76	LP	−21.65362	−67.80825	2.09	−4.34		
Platystromatolite	PG17-72	LP	−21.65554	−67.81396	2.59	−2.60	0.1038	18,197 (± 52) *
	PG17-75.2	LP	−21.65362	−67.80825	3.96	−3.73		
	PG17-75.1	LP	−21.65362	−67.80825	3.51	−5.33		
Fusoid-bearing mud	PG2-33	L	−21.62555	−67.74513	−0.65	−1.78		
	PG2-2	L	−21.6957	−67.80938	−2.45	−2.06		
	PG17-84b	L	−21.69645	−67.80445	−2.04	−3.44		
	PG17-81	L	−21.6837	−67.8222	−0.60	−3.20		
	PG2-16	L	−21.6975	−67.7475	−1.41	−1.52		

* ^{14}C ages were calculated as $-8033 \cdot \ln(F^{14}C)$ [41], ages considered before 1950 (yr BP = year before present), after correction of the fractionation produced by the spectrometer. ^{14}C ages cannot be used for dating due to the incorporation of fossil carbon (see Section 5—Discussion).

Anhedral calcite, in mud precipitating in the hydrothermal La Salsa system recorded lower isotope values, from −1.4‰ to +2.1‰ for $\delta^{13}C_{carb}$ and −11.5‰ to −5.8‰ for $\delta^{18}O_{carb}$. Pisolites, collected from ephemeral and perennial pools on the upper platform, recorded intermediate values compared to La Salsa, ranging from +1.3‰ to +5.4‰ for $\delta^{13}C_{carb}$ and from −9.3‰ to −3.7‰ for $\delta^{18}O_{carb}$. Fusoid mud from the lower and upper platforms can be distinguished from pisolites, with slightly lower values for $\delta^{13}C_{carb}$ (from +1.3‰ to +3.5‰), but higher for $\delta^{18}O_{carb}$ (from −5.9‰ to −3.1‰). Platystromatolites presented similar values, ranging from +2.6‰ to +4.0‰ for $\delta^{13}C_{carb}$, and from −5.3‰ to −2.6‰ for $\delta^{18}O_{carb}$. Palmatoid concretions recorded a much broader isotope amplitude, ranging from +0.6‰ to +11.5‰ for $\delta^{13}C_{carb}$ and from −8.1‰ to −2‰ for $\delta^{18}O_{carb}$, close to the amplitude observed over the entire La Salsa transect. Two groups of values can nevertheless be identified: the submerged part, with lower values (+0.6‰ to +2.3‰ for $\delta^{13}C_{carb}$ and −8.1‰ to −7.2‰ for $\delta^{18}O_{carb}$), and the subaerially exposed part, with higher values (+6.1‰ to +11.5‰ for $\delta^{13}C_{carb}$ and −5.1‰ to −2.0‰ for $\delta^{18}O_{carb}$). Fusoid-bearing mud from the saline lake appeared very different from the other facies, with $\delta^{13}C_{carb}$ values ranging from −2.5‰ to −0.6‰, and $\delta^{18}O_{carb}$ values ranging from −3.4‰ to −1.5‰.

4.3.2. Fraction Modern Carbon ($F^{14}C$) from Modern Carbonates

In five of the facies analyzed, the fraction modern ($F^{14}C$) was very low (Table 3). In La Salsa, the $F^{14}C$ value was 0.0469 for a proximal microbialite (Z1—mushroom-like), increasing to 0.1068 (2.3 times higher) in a distal microbialite (Z4—shrub). The fraction modern measured for concretions growing in pools was also low, with an $F^{14}C$ value of 0.0639 for a pisolite and 0.0333 for a palmatoid concretion. A higher value of 0.1038 was recorded for a platystromatolite.

5. Discussion

5.1. Using Isotopes for Carbonate Dating in Volcanic Settings

Comparison between the U–Th ages from the carbonate platform and the ^{14}C ages from the modern deposits showed that the ^{14}C ages were globally older than the U–Th ages, even though these modern carbonate deposits are stratigraphically higher than the carbonate platform.

In the uppermost layers of the actively precipitating microbialites at the edge of the central pool of La Salsa spring, the recorded fraction modern was very low ($F^{14}C$ = 0.0469). The age calculated from this value (24.5 ka) would be inconsistent, as modern carbonates are associated with the modern development of microbial mats and ongoing carbonate precipitation. In addition, modern carbonates develop above the Holocene carbonate platform, dated at 1–2 ka by U–Th, and so they should be younger. The anomalous ^{14}C ages were coherent with the incorporation of "dead carbon", as the pCO_2 estimated in these systems was approximately 60.3 to 389 mbar [16], that is to say 260 to 1676 times greater than atmospheric pCO_2 (considering an atmospheric pCO_2 of 407.18 ppm at 0 m, and so 232 ppm (0.232 mbar) at 4500 m on March 2017, source: NOAA). Such high hypogean pCO_2 would trigger major dilution of atmospheric CO_2 in the laguna water system (e.g., [42]). This overestimate results from the incorporation of metamorphic or magmatic CO_2 or possibly of CO_2 from the recycling of older carbonates in the laguna [16,42,43]. Caution is therefore recommended in settings where hypogean CO_2 emissions are present.

5.2. Factors Controlling the Isotope Record in Each Hydrological Setting

Each part of the complex Pastos Grandes hydrological system (i.e., piedmont springs, ephemeral streams, hydrothermal springs, ephemeral or perennial pools, and an ephemeral saline lake) has a specific chemical composition [16], leading to different types of mineralization (Figure 8A). The origin of chemical elements and gas in the system, particularly calcium and CO_2, were investigated by Muller et al. [16]. They determined that the main driver for the precipitation of modern carbonates at Pastos Grandes was the deeply sourced CO_2 surging from hydrothermal springs and partly deriving from the mantle (47%). Additionally, the modeling provided by their study showed that fluid circulation

under high PCO_2 (20 bar) and high temperature (~225 °C) resulted in the alteration of the volcanic bedrock, which contains Ca-rich minerals (mainly feldspars). Therefore, hydrothermal springs can be considered as the main providers of solutes, and thus as reference water compositions. Carbonate mineralization is mainly restricted to the primary solute providers (i.e., hydrothermal springs) and receivers (i.e., pools and the lake). These three hydrological environments (Figure 8B) have similar chemical compositions with different levels of concentration, and some temporal variability related to meteoric input and evaporation.

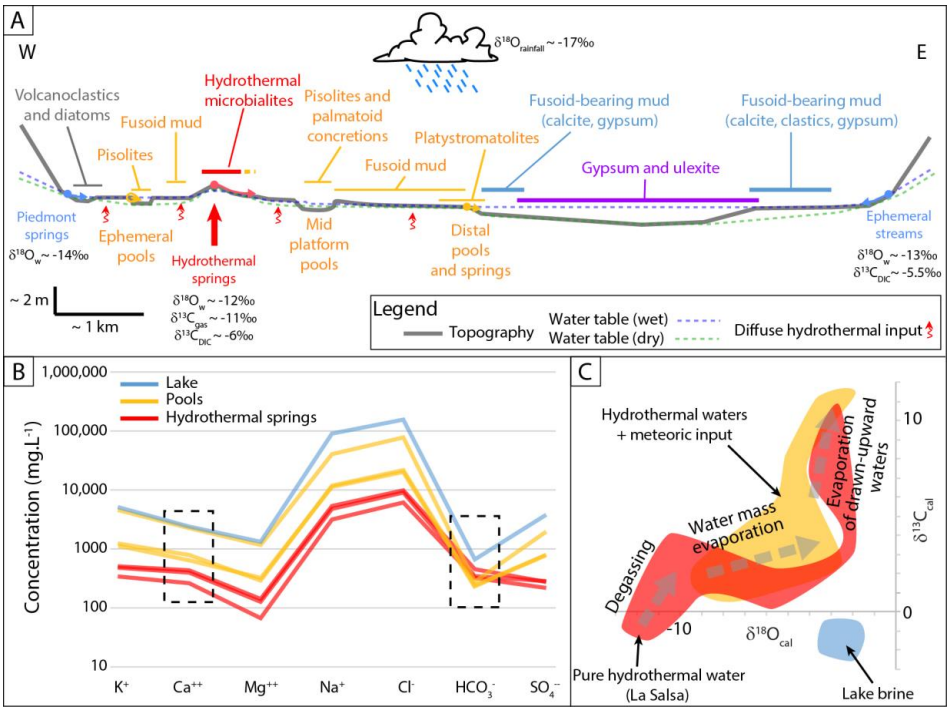

Figure 8. (**A**) Simplified transect of macrofacies distribution in Pastos Grandes. Fluid inputs were characterized by their C and O stable isotope signatures. (**B**) A Schoeller diagram of ionic composition and concentration for specific parent fluids involved in carbonate precipitation. (**C**) A simplified isotope cross plot showing a range of values for each fluid, and processes triggering isotope evolution.

Compared with hydrothermal profiles, the profiles for both the pools and the lake show the same relative decrease in concentration for two solutes, Ca^{++} and HCO_3^-, implying that these solutes have been consumed by carbonate precipitation.

5.2.1. Pure Hydrothermal Systems

Pure hydrothermal systems are places where hydrothermal inputs rise to the surface, characterized by hot, acidic waters, high pCO_2, and low isotope compositions ($\delta^{18}O_{H2O}$ approximately −12‰ and $\delta^{13}C_{CO2(gas)}$ approximately −11.4‰ [16]). In the system under study, La Salsa, the amplitude of isotope values recorded from microbialites was large (12.2‰ for $\delta^{13}C$; 10.6‰ for $\delta^{18}O$), over a short distance (~280 m), and close to the full range of values measured in Pastos Grandes (Figure 8C). A previous study showed that microbialite morphology and distribution in La Salsa was primarily controlled by CO_2 degassing, temperature decrease, microbial photosynthesis, and substrate nature [14].

The $\delta^{13}C_{carb}$ values for calcite precipitating as ledge microbialites on the edges of the central pool were −0.8‰, higher than the $\delta^{13}C_{gas}$ (about −11.2‰ PDB) and $\delta^{13}C_{DIC}$ (about −6‰ PDB) values [16]. The abundance of CO_2 in the pool favors degassing, triggering isotope fractionation between the gas–liquid phases and liquid–mineral phases, thus explaining the higher values recorded by the calcite in the ledge microbialites [44–46].

The $\delta^{18}O_{carb}$ value measured at the edge of the central pool (−12.5‰ PDB) was controlled by the $\delta^{18}O_{water}$. Applying the equation of Friedman and O'Neil [47], with a $\delta^{18}O_{water}$ of −11.4‰ SMOW (Standard Mean Ocean Water) [16] and a precipitation temperature of 43 °C, the $\delta^{18}O_{carb}$ value calculated for the same microbialites would be lower (−16.7‰ PDB). This 4.2‰ difference corresponds to the non-equilibrium calcite–water fractionation observed in most other hydrothermal systems around the world, due to kinetic effects, particularly in conjunction with CO_2 degassing [45,46]. This observation confirms the difficulty of using $\delta^{18}O_{carb}$ for paleotemperature calculation in hydrothermal contexts with abundant CO_2.

From Zone 1 (proximal) to Zone 4 (distal) of the hydrothermal system, an increase was observed in $\delta^{13}C_{carb}$ and $\delta^{18}O_{carb}$ values measured in microbialites. Nevertheless, the increase in $\delta^{13}C$ was relatively low and may have resulted from a rapid transfer of water from the channel to the distal area, as the water flow was relatively high. A similar increase was also observed in many travertine-producing hydrothermal springs, usually triggered by CO_2 degassing and temperature decrease (e.g., [44,46,48]). Zone 4 showed an abrupt increase in $\delta^{13}C_{carb}$ values (+7.1‰ to +10.7‰ PDB), which were uncommonly elevated in comparison with other hydrothermal systems. These high $\delta^{13}C_{carb}$ values were associated with the presence of millimetric branches at the top of the shrubs. This branching mineralization resulted from subaerial exposure, as water was drawn upward by frequent water–surface oscillations, and capillary rise through microbial mats [14,49]. Subaerial exposure and strong evaporation could trigger ^{13}C enrichment at the top of shrubby morphologies. Isotope enrichment has seldom been documented in shrub morphologies in hydrothermal settings. Although similar morphologies in Bahía Concepción (Mexico), with high $\delta^{13}C_{carb}$ values, have been explained by CO_2 degassing [50], it is possible that subaerial exposure and evaporation may have also played a role in this intertidal context. For the fraction modern, the value (F(^{14}C): 0.1068) measured in a shrub in Zone 4 was 2.28 times higher than the value measured in a ledge in Zone 1 (F(^{14}C): 0.0469). This increase suggests greater incorporation of atmospheric carbon in the carbonate precipitated in Zone 4. Despite this increase, the fraction modern remains relatively low when compared to the atmospheric value measured in 2010 ($F^{14}C$: 1.05; [51]), indicating that "dead carbon" remains the main source of CO_2 incorporated in carbonates.

5.2.2. Combined Hydrothermal and Meteoric Inputs

The pools between the hydrothermal springs and the saline lake are fed by hydrothermal water, more or less diluted by meteoric inputs (Figure 8A). The amplitude of isotope values (7.3‰ PDB for $\delta^{18}O_{carb}$ and 10.6‰ PDB for $\delta^{13}C_{carb}$) for the main carbonate macrostructures found on the platform (pisolites, palmatoids, platystromatolites, and fusoid muds) is lower than for the pure hydrothermal system, with higher minimum values (Figure 8C). The broad range of $\delta^{18}O_{carb}$ values measured in pisolites (from −9.3‰ to −3.7‰ PDB), which precipitated during the same period, could originate from microenvironmental variations, with different inputs from meteoric and hydrothermal waters, but also from the stability of the pool, which depends on whether and how much it is fed by waters, but also variations in the evaporation rate among the pools, which consequently induces fluctuations in $\delta^{18}O_{carb}$ [52]. The $\delta^{18}O_{carb}$ values measured in platystromatolites and fusoid muds were more positive than those observed in pisolites, suggesting a higher rate of evaporation.

Palmatoid concretions only developed in persistent pools lying between the upper and the lower platforms, in association with pisolites. The values for $\delta^{18}O_{carb}$ and $\delta^{13}C_{carb}$ measured in the submerged part of these palmatoids were similar to the most negative values measured in pisolites (Figure 7A), suggesting subaqueous precipitation for these carbonates. By contrast, the values for $\delta^{18}O_{carb}$ and $\delta^{13}C_{carb}$ measured from the subaerially exposed part of the concretions were much higher than even the highest values for pisolites (Figure 7A). The branching morphology of these palmatoid concretions is very similar to that of the shrub microbialites from hydrothermal springs, with equally high $\delta^{18}O_{carb}$ and $\delta^{13}C_{carb}$ values. In both cases, water was drawn upward by water–surface oscillations, but the associated process for shrubs was capillary rise through microbial mats [14], while for palmatoid concretions, the process was wind-induced spray [12]. Such positive shifts have already been described for other

carbonate deposits, including vadose crusts and cements near marine coastlines [53], stalagmites [54], and carbonate precipitated in mountain streams [55]. Coupled with strong evaporation, spray-induced processes accentuate the release of light CO_2 in strongly alkaline waters, greatly increasing both $\delta^{13}C_{carb}$ and $\delta^{18}O_{carb}$ values.

5.2.3. The Saline Lake, Mainly Fed by Meteoric Waters

Slightly negative $\delta^{13}C_{carb}$ and $\delta^{18}O_{carb}$ values were recorded in the fusoid-bearing mud in the eastern part of the laguna (Figure 8C), with an ephemeral central lake that is strongly affected by the arid climate, triggering evaporation over the year. The slightly negative $\delta^{18}O_{carb}$ values observed here were similar to the highest $\delta^{18}O_{carb}$ values recorded on the carbonate platform (i.e., fusoid mud, shrubs, palmatoid concretions, and platystromatolites), which are interpreted as having precipitated from strongly evaporated waters. This result suggests that the lake water was also strongly evaporated when the fusoid-bearing mud precipitated. The lake is mainly fed by meteoric inputs with a very low $\delta^{18}O_{water}$ value (−17‰), supplemented by underground, non-evaporated, hydrothermal waters, with a slightly higher, but still negative $\delta^{18}O_{water}$ value (−11.4‰). The slightly negative $\delta^{13}C_{carb}$ values observed here were similar to the most negative $\delta^{13}C_{carb}$ values found at the outlet of hydrothermal springs. They are best explained by two factors: (i) the extremely efficient C-isotope equilibrium of the dissolved inorganic carbon in the lake water with the atmospheric CO_2 because of the shallowness of the lake, which evaporates completely every year, and (ii) the addition of low $\delta^{13}C_{DIC}$ in the lake by underground hydrothermal inputs and organic matter mineralization.

5.3. Laguna Pastos Grandes in Comparison with Other Andean Contexts

Laguna Pastos Grandes carbonates record a great range of values for both $\delta^{13}C$ (13.9‰) and $\delta^{18}O$ (11.1‰), associated with three main depositional environments. This dispersion is among the highest known in the Central Andes (Figure 9) and elsewhere (Figure S3). A greater dispersion of isotope values has only been observed at Laguna Negra in Argentina (17.3% in $\delta^{13}C$; 11.3‰ in $\delta^{18}O$) where the amplitude results not only from temporal variations in moisture, which are recorded in microbialites (temporal amplitude varying from 4‰ to 11‰ for $\delta^{13}C$, and 3‰ to 8‰ for $\delta^{18}O$) [9], but also from spatial controls driven by the diversity of depositional environments (inlet mixing with lake, or lake alone) [9,56]. Differences in depositional environments strongly affect the isotope record, even over short distances.

At Pastos Grandes, depositional environments fed by pure hydrothermal or mixed hydrothermal–meteoric waters record markedly negative $\delta^{18}O$ values, contrasting strongly with the higher values recorded in carbonates at other hydrothermal Andean sites (i.e., Las Peladas and Las Coladas, Argentina) [4]. Higher $\delta^{18}O$ values indicate either a difference in initial isotope composition at the spring outlet, or enrichment in heavy isotopes further from the outlet, caused by decreasing temperatures and increased evaporation. The most positive $\delta^{13}C$ values, found in carbonates deriving from hydrothermal fluids at Pastos Grandes, were close to the most positive values obtained in other Andean hydrothermal settings [4]. At both Las Coladas and Las Peladas, the origin of these high values, recorded in laminated travertines, was attributed to intense CO_2 release. In contrast, at Pastos Grandes, the high $\delta^{13}C$ values were measured in isolated, partially emerged objects (palmatoid and shrub concretions), far from the spring outlet. In this subaerial depositional context, the high $\delta^{18}O$ values resulted from different processes, recorded exclusively at the facies scale: the evaporation of alkaline waters drawn upward by frequent water–surface oscillation, and capillary rise in the microbial mat.

In the ephemeral central lake of Pastos Grandes, the slightly negative values (between −2.5‰ and −0.6‰ for $\delta^{13}C$; −3.4‰ and −1.5‰ for $\delta^{18}O$) were low compared to values for other Andean lacustrine carbonates (including mud and microbialites), particularly the values for $\delta^{13}C$. In fact, other Andean lakes frequently record higher values, with some almost reaching +10‰ for both $\delta^{13}C$ and $\delta^{18}O$ (e.g., Laguna Negra and El Peinado in Argentina, and Laguna Seca and Laguna del Negro Francisco in Chile; Figure 9). Even though some latitudinal variations in precipitation exist, which may

induce some changes in the initial $\delta^{18}O$ coming from rainfall, the strong evaporation ruling over the Central Andes affects the isotope record, inducing very positive $\delta^{18}O$ values, (e.g., [56]), enhanced by the perennial character of the lakes with a relatively long water residence time [4,52,57]. In such lakes, partial evaporation favors the escape of light oxygen isotopes (^{16}O), so that heavy oxygen isotopes (^{18}O) accumulate in lake water over the years. This ^{18}O enrichment is then recorded in the carbonates. In Andean systems, the elevated groundwater CO_2 concentration, common in volcanic areas, can reach lakes, even if superficial markers of hypogean input (e.g., travertine) are not always observed [11,42]. The major degassing of light CO_2 of the lake has been shown to trigger ^{13}C enrichment in water and carbonates [43,56]. The strong enrichment in heavy carbon isotopes in carbonates may track the rise of CO_2 in systems influenced by volcanism, even in the quiescent stage. These abiotic processes are also enhanced by the long water residence time in perennial lakes that favors storage of heavy isotopes such as oxygen [9,43]. These values can be further amplified by photosynthesis and microbial methanogenesis activities [11]. In the case of Pastos Grandes, the origin of CO_2 in the lake results either from hydrothermal inputs or from the air–water equilibrium. However, as the lake water completely evaporates every year, the short residence time prevents significant enrichment in ^{13}C and ^{18}O, thus explaining the lower $\delta^{13}C_{carb}$–$\delta^{18}O_{carb}$ values observed. Moreover, as Pastos Grandes is an endoreic lake, the short water residence time would also explain the absence of covariance between $\delta^{13}C_{carb}$ and $\delta^{18}O_{carb}$, often used to identify closed-basin settings [58].

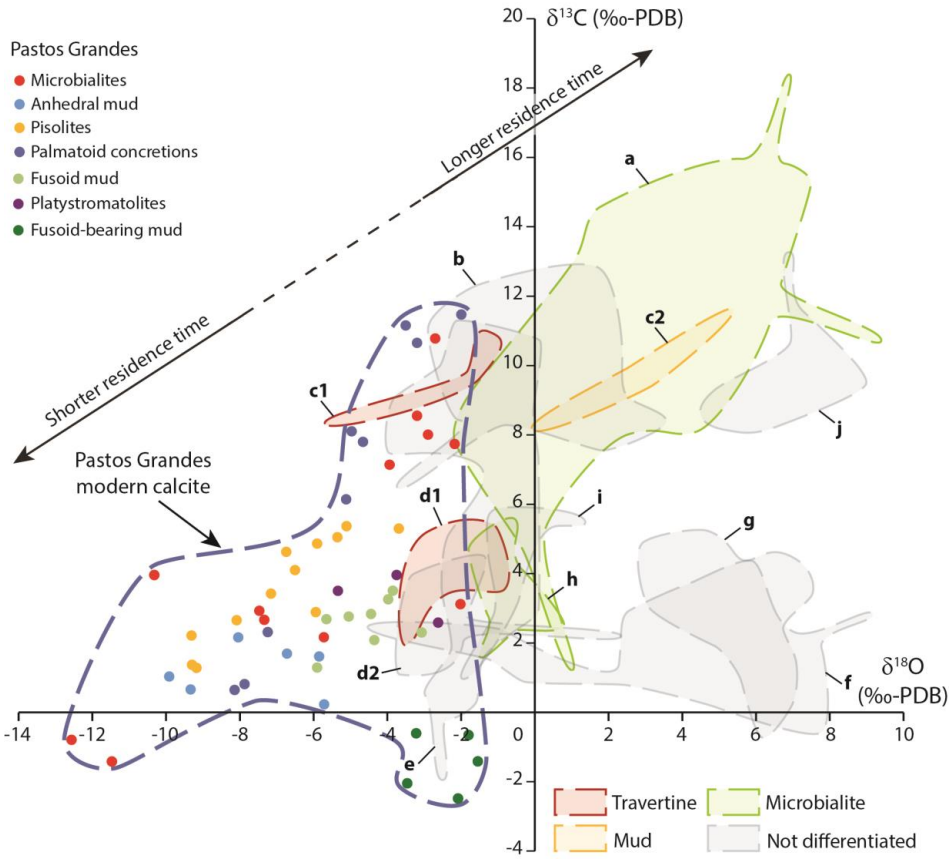

Figure 9. $\delta^{18}O$–$\delta^{13}C$ cross-plot comparing carbonates from Laguna Pastos Grandes (dashed line, in blue) and recent to present-day carbonates from other Andean locations, influenced by the same arid, high-altitude climate, as follows: a—Laguna Negra, Argentina [9,11]; b—Laguna Seca, Chile [3]; c1,2—Las Coladas, Argentina [4]; d1,2—Las Peladas, Argentina [4]; e—Lake Chungará, Argentina [59]; f—Laguna del Negro Francisco, Chile [3]; g—Laguna Miscanti, Chile [3]; h—Tauca and Coipasa lake highstand, Bolivia [6]; i—San Francisco, Argentina [4]; j—El Peinado [4]. Recent to present-day locations with high $\delta^{13}C_{carb}$ values suggest volcanic influence (CO_2 input).

6. Conclusions

Laguna Pastos Grandes is a palustrine-to-lacustrine site developing in a quiescent volcanic caldera with abundant ongoing carbonate sedimentation, diversified macrofacies, and several parent waters. Seven different carbonate facies were identified along a platform—lake transect. The sedimentological and hydrological diversity is accompanied by great amplitude in $\delta^{13}C_{carb}$ and $\delta^{18}O_{carb}$ values, unusual for modern continental environments, whether in the Altiplano or elsewhere in the world. This study shows that several extrinsic factors play an important role in the resulting isotope record in carbonates:

- The initial isotope composition of parent waters (purely hydrothermal, mixed hydrothermal–meteoric, or meteoric-dominated) is the main extrinsic factor triggering differences in carbon and oxygen isotope values recorded in carbonates from different depositional environments;
- By moving away from hydrothermal inputs, isotopes are increasingly influenced by aridity, causing evaporation, enhanced by wind action, and by capillary rise through the microbial mat, thus triggering major carbon and oxygen isotope enrichments;
- The short water residence time explains the main difference between Laguna Pastos Grandes (with a slightly negative isotope signature of carbonates) and the other Andean lakes (with positive isotope signatures of carbonates), which are all under the influence of an arid climate. The isotope convergence toward high $\delta^{13}C_{carb}$ from Pastos Grandes and several other Andean lakes is triggered by volcanic CO_2 input, and so carbon isotopes can be particularly useful to identify ancient carbonate systems affected by volcanic activity. However, controlling factors triggering ^{13}C enrichment in carbonates corresponded to large-scale processes for Andean lakes (long residence time), and facies-scale processes for Pastos Grandes (evaporation of drawn-upward waters);
- The fraction modern $F^{14}C$ was modified in volcanic settings by the injection of "dead carbon" into the system. This makes ^{14}C dating of carbonates particularly unreliable in Andean lakes enriched in volcanic CO_2.

Laguna Pastos Grandes is an interesting natural laboratory, where isotope variations can be observed in an active system, in a limited area, over a very short period (compared to geological time scales). The extrinsic processes observed here could well have affected carbonate isotope signatures in ancient subaerial carbonate deposits in continental settings under volcanic influence.

Supplementary Materials: The following are available online at http://www.mdpi.com/2075-163X/10/11/989/s1, Figure S1: Laguna Pastos Grandes sedimentary system, showing sampling sites (modern carbonates) used for isotope measurements; Table S1: Location of samples from the carbonate platform used for U–Th dating; Figure S2: Lake level fluctuations from 2000 to 2019; Figure S3: $\delta^{18}O/\delta^{13}C$ values, recorded in modern-to-recent carbonates, precipitating in hydrothermal to lacustrine settings in Africa (in red), Europe (in yellow), and North America (in green).

Author Contributions: Conceptualization, C.B.; validation, C.B., C.D., and E.V.; investigation, C.B., C.D., E.V., E.M., B.G., and E.G.; writing—original draft preparation, C.B.; writing—review and editing, C.B., C.D., E.V., E.M., M.A., A.V., and E.C.G.; visualization, C.B.; supervision, C.B., C.D., E.V., A.V., and E.C.G.; project administration, A.V. and E.C.G. All authors have read and agreed to the published version of the manuscript.

Funding: This research received no external funding.

Acknowledgments: This study was a contribution from the French Total R&D (supervisor: Emmanuelle Poli), the SEDS team of the Biogéosciences Laboratory (Dijon, France), and the I-site project UB18016-BGS-IS. The authors express their gratitude to the Bolivian Total E&P team (Olivier-Daniel Moreau, Jean-Pierre Meunier, Rozmery Cuellar, and Serge Nicoletis) for technical support in Bolivia, and Marco Chavez for accompanying them during the field expedition. They thank the Sanda Andina Company for logistical contributions on site. They are grateful to Chloé Morales for the fruitful discussions on ikaite, to Théophile Cocquerez (Biogéosciences Laboratory) for stable isotope analyses, and to Stephan Borensztain (IPGP) for SEM images. The authors are also grateful to the academic editor Monica Piochi and the two anonymous reviewers for their useful comments.

Conflicts of Interest: The authors declare no conflict of interest.

References

1. Gasse, F.; Fontes, J.-C. Palaeoenvironments and palaeohydrology of a tropical closed lake (Lake Asal, Djibouti) since 10,000 yr B.P. *Palaeogeogr. Palaeoclimatol. Palaeoecol.* **1989**, *69*, 67–102. [CrossRef]
2. Benson, L.; White, L.D.; Rye, R. Carbonate deposition, Pyramid Lake Subbasin, Nevada: 4. Comparison of the stable isotope values of carbonate deposits (tufas) and the Lahontan lake-level record. *Palaeogeogr. Palaeoclimatol. Palaeoecol.* **1996**, *122*, 45–76. [CrossRef]
3. Schwalb, A.; Burns, S.J.; Kelts, K. Holocene environments from stable isotope stratigraphy of ostracods and authigenic carbonate in Chilean Altiplano Lakes. *Palaeogeogr. Palaeoclimatol. Palaeoecol.* **1999**, *148*, 153–168. [CrossRef]
4. Valero-Garcés, B.L.; Arenas, C.; Delgado-Huertas, A. Depositional environments of Quaternary lacustrine travertines and stromatolites from high-altitude Andean lakes, northwestern Argentina. *Can. J. Earth Sci.* **2001**, *38*, 1263–1283. [CrossRef]
5. McDermott, F. Palaeo-climate reconstruction from stable isotope variations in speleothems: A review. *Quat. Sci. Rev.* **2004**, *23*, 901–918. [CrossRef]
6. Blard, P.-H.; Sylvestre, F.; Tripati, A.K.; Claude, C.; Causse, C.; Coudrain, A.; Condom, T.; Seidel, J.-L.; Vimeux, F.; Moreau, C.; et al. Lake highstands on the Altiplano (Tropical Andes) contemporaneous with Heinrich 1 and the Younger Dryas: New insights from ^{14}C, U–Th dating and δ^{18}O of carbonates. *Quat. Sci. Rev.* **2011**, *30*, 3973–3989. [CrossRef]
7. Rouchy, J.M.; Servant, M.; Fournier, M.; Causse, C. Extensive carbonate algal bioherms in upper Pleistocene saline lakes of the central Altiplano of Bolivia. *Sedimentology* **1996**, *43*, 973–993. [CrossRef]
8. Sylvestre, F.; Servant, M.; Servant-Vildary, S.; Causse, C.; Fournier, M.; Ybert, J.-P. Lake-Level Chronology on the Southern Bolivian Altiplano (18°–23°) during Late-Glacial Time and the Early Holocene. *Quat. Res.* **1999**, *51*, 54–66. [CrossRef]
9. Buongiorno, J.; Gomez, F.J.; Fike, D.A.; Kah, L.C. Mineralized microbialites as archives of environmental evolution, Laguna Negra, Catamarca Province, Argentina. *Geobiology* **2019**, *17*, 199–222. [CrossRef]
10. Ballivián, O.; Risacher, F. *Los Salares del Altiplano Boliviano: Métodos de Estudio y Estimación Económica*; ORSTOM: Paris, France, 1981; 246p.
11. Gomez, F.J.; Kah, L.C.; Bartley, J.K.; Astini, R.A. Microbialites in a high-altitude andean lake: Multiple controls on carbonate precipitation and lamina accretion. *Palaios* **2014**, *29*, 233–249. [CrossRef]
12. Risacher, F.; Eugster, H.P. Holocene pisoliths and encrustations associated with spring-fed surface pools, Pastos Grandes, Bolivia. *Sedimentology* **1979**, *26*, 253–270. [CrossRef]
13. Jones, B.; Renaut, R.W. Crystal fabrics and microbiota in large pisoliths from Laguna Pastos Grandes, Bolivia. *Sedimentology* **1994**, *41*, 1171–1202. [CrossRef]
14. Bougeault, C.; Vennin, E.; Durlet, C.; Muller, E.; Mercuzot, M.; Chavez, M.; Gérard, E.; Ader, M.; Virgone, A.; Gaucher, E.C. Biotic-abiotic Influences on Modern Ca–Si-Rich Hydrothermal Spring Mounds of the Pastos Grandes Volcanic Caldera (Bolivia). *Minerals* **2019**, *9*, 380. [CrossRef]
15. Soria, M.N.; Lencina, A.I.; Saona, L.A.; Stepanenko, T.M.; Colla, M.F.; Farías, M.E. *New Different Modern Microbialites Deposits in Puna of Catamarca, Argentine*; M-Fed Congress: Dijon, France, 2019.
16. Muller, E.; Gaucher, E.C.; Durlet, C.; Moquet, J.; Moreira, M.; Rouchon, V.; Louvat, P.; Bardoux, G.; Noirez, S.; Bougeault, C.; et al. The Origin of Continental Carbonates in Andean Salars: A Multi-Tracer Geochemical Approach in Laguna Pastos Grandes (Bolivia). *Geochim. Cosmochim. Acta* **2020**, *279*, 220–237. [CrossRef]
17. Martinod, J.; Husson, L.; Roperch, P.; Guillaume, B.; Espurt, N. Horizontal subduction zones, convergence velocity and the building of the Andes. *Earth Planet. Sci. Lett.* **2010**, *299*, 299–309. [CrossRef]
18. Thorpe, R.S.; Francis, P.W. Variations in Andean andesite compositions and their petrogenetic significance. *Tectonophysics* **1979**, *57*, 53–70. [CrossRef]
19. Isacks, B.L. Uplift of the Central Andean Plateau and Bending of the Bolivian Orocline. *J. Geophys. Res.* **1988**, *93*, 3211–3231. [CrossRef]
20. De Silva, S.L. Altiplano–Puna volcanic complex of the central Andes. *Geology* **1989**, *17*, 1102–1106. [CrossRef]
21. Salisbury, M.J.; Jicha, B.R.; de Silva, S.L.; Singer, B.S.; Jiménez, N.C.; Ort, M.H. ^{40}Ar/^{39}Ar chronostratigraphy of Altiplano–Puna volcanic complex ignimbrites reveals the development of a major magmatic province. *Geol. Soc. Am. Bull.* **2011**, *123*, 821–840. [CrossRef]

22. De Silva, S.; Zandt, G.; Trumbull, R.; Viramonte, J.G.; Salas, G.; Jiménez, N. Large ignimbrite eruptions and volcano-tectonic depressions in the Central Andes: A thermomechanical perspective. *Geol. Soc. Lond. Spec. Publ.* **2006**, *269*, 47–63. [CrossRef]
23. Kay, S.M.; Coira, B.L. Shallowing and steepening subduction zones, continental lithospheric loss, magmatism, and crustal flow under the central Andean Altiplano-Puna Plateau. In *Backbone of the Americas: Shallow Subduction, Plateau Uplift, and Ridge and Terrane Collision*; Kay, S.M., Ramos, V.A., Dickinson, W.R., Eds.; The Geological Society of America: Boulder, CO, USA, 2009; Volume 204, pp. 229–260.
24. De Silva, S.L.; Kay, S.M. Turning up the Heat: High-Flux Magmatism in the Central Andes. *Elements* **2018**, *14*, 245–250. [CrossRef]
25. Chmielowski, J.; Zandt, G.; Haberland, C. The Central Andean Altiplano-Puna Magmatic Body. *Geophys. Res. Lett.* **1999**, *26*, 783–786. [CrossRef]
26. Ward, K.M.; Zandt, G.; Beck, S.L.; Christensen, D.H.; McFarlin, H. Seismic imaging of the magmatic underpinnings beneath the Altiplano-Puna volcanic complex from the joint inversion of the surface wave dispersion and receiver functions. *Earth Planet. Sci. Lett.* **2014**, *404*, 43–53. [CrossRef]
27. Kaiser, J.F.; de Silva, S.; Schmitt, A.K.; Economos, R.; Sunagua, M. Million-year melt-presence in monotonous intermediate magma for a volcanic-plutonic assemblage in the Central Andes: Contrasting histories of crystal-rich and crystal-poor super-sized silicic magmas. *Earth Planet. Sci. Lett.* **2017**, *457*, 73–86. [CrossRef]
28. Peel, M.C.; Finlayson, B.L.; McMahon, T.A. Updated world map of the Köppen-Geiger climate classification. *Hydrol. Earth Syst. Sci.* **2007**, *4*, 439–473. [CrossRef]
29. Iltis, A.; Risacher, F.; Servant–Vildary, S. Contribution à l'étude hydrobiologique des lacs salés du sud de l'Altiplano bolivien. *Rev. Hydrobiol. Trop.* **1984**, *17*, 259–273.
30. Servant-Vildary, S.; Roux, M. Multivariate analysis of diatoms and water chemistry in Bolivian saline lakes. *Hydrobiologia* **1990**, *197*, 267–290. [CrossRef]
31. Risacher, F.; Fritz, B. Geochemistry of Bolivian salars, Lipez, southern Altiplano: Origin of solutes and brine evolution. *Geochim. Cosmochim. Acta* **1991**, *55*, 687–705. [CrossRef]
32. Ghaleb, B.; Falguères, C.; Carlut, J.; Pozzi, J.-P.; Mahieux, G.; Boudad, L.; Rousseau, L. Timing of the Brunhes-Matuyama transition constrained by U-series disequilibrium. *Sci. Rep.* **2019**, *9*, 6039. [CrossRef]
33. Edwards, R.L.; Chen, J.H.; Wasserburg, G.J. 238U–234U–230Th–232Th systematics and the precise measurement of time over the past 500,000 years. *Earth Planet. Sci. Lett.* **1987**, *81*, 175–192. [CrossRef]
34. Ludwig, K.R.; Paces, J.P. Uranium-series dating of pedogenic silica and carbonate, Crater Flat, Nevada. *Geochim. Cosmochim. Acta* **2002**, *66*, 487–506. [CrossRef]
35. St-Jean, G.; Kieser, W.E.; Crann, C.A.; Murseli, S. Semi-Automated Equipment for CO_2 Purification and Graphitization at the A.E. Lalonde Laboratory (Ottawa, Canada). *Radiocarbon* **2017**, *59*, 941–956. [CrossRef]
36. Placzek, C.; Patchett, P.J.; Quade, J.; Wagner, J.D.M. Strategies for successful U-Th dating of paleolake carbonates: An example from the Bolivian Altiplano. *Geochem. Geophys. Geosyst.* **2006**, *7*, Q05024. [CrossRef]
37. Rucker, J.B.; Carver, R.E. A Survey of the Carbonate Mineralogy of Cheilostome Bryozoa. *J. Paleontol.* **1969**, *43*, 791–799.
38. Geyh, M.A.; Grosjean, M.; Núñez, L.; Schotterer, U. Radiocarbon Reservoir Effect and the Timing of the Late-Glacial/Early Holocene Humid Phase in Atacama Desert (Northern Chile). *Quat. Res.* **1999**, *52*, 143–153. [CrossRef]
39. Oehlerich, M.; Mayr, C.; Griesshaber, E.; Lücke, A.; Oeckler, O.M.; Ohlendorf, C.; Schmahl, W.W.; Zolitschka, B. Ikaite precipitation in a lacustrine environment—Implications for palaeoclimatic studies using carbonates from Laguna Potrok Aike (Patagonia, Argentina). *Quat. Sci. Rev.* **2013**, *71*, 46–53. [CrossRef]
40. Ohlendorf, C.; Fey, M.; Massaferro, J.; Haberzettl, T.; Laprida, C.; Lücke, A.; Maidana, N.; Mayr, C.; Oehlerich, M.; Ramón Mercau, J.; et al. Late Holocene hydrology inferred from lacustrine sediments of Laguna Cháltel (southeastern Argentina). *Palaeogeogr. Palaeoclimatol. Palaeoecol.* **2014**, *411*, 229–248. [CrossRef]
41. Stuiver, M.; Polach, H.A. Discussion Reporting of ^{14}C Data. *Radiocarbon* **1977**, *19*, 355–363. [CrossRef]
42. Mao, X.; Wang, H.; Feng, L. Impact of additional dead carbon on the circulation estimation of thermal springs exposed from deep-seated faults in the Dongguan basin, southern China. *J. Volcanol. Geotherm. Res.* **2018**, *361*, 1–11. [CrossRef]
43. Valero-Garcés, B.L.; Delgado-Huertas, A.; Ratto, N.; Navas, A. Large ^{13}C enrichment in primary carbonates from Andean Altiplano lakes, northwest Argentina. *Earth Planet. Sci. Lett.* **1999**, *171*, 253–266. [CrossRef]

44. Gonfiantini, R.; Panichi, C.; Tongiorgi, E. Isotopic disequilibrium in travertine deposition. *Earth Planet. Sci. Lett.* **1968**, *5*, 55–58. [CrossRef]
45. Pentecost, A. *Travertine*; Springer: Berlin, Germany, 2005; 445p.
46. Kele, S.; Özkul, M.; Fórizs, I.; Gökgöz, A.; Baykara, M.O.; Alçiçek, M.C.; Németh, T. Stable isotope geochemical study of Pamukkale travertines: New evidences of low-temperature non-equilibrium calcite-water fractionation. *Sediment. Geol.* **2011**, *238*, 191–212. [CrossRef]
47. Friedman, I.; O'Neil, J.R. Compilation of stable isotope fractionation factors of geochemical interest. In *Data of Geochemistry*, 6th ed.; Geological Survey Professional Paper 440-KK; Fleische, M., Ed.; U.S. Geological Survey: Washington, DC, USA, 1977; pp. KK1–KK12.
48. Fouke, B.W.; Farmer, J.D.; des Marais, D.J.; Pratt, L.; Sturchio, N.C.; Burns, P.C.; Discipulo, M.K. Depositional facies and aqueous-solid geochemistry of travertine-depositing hot springs (Angel Terrace, Mammoth Hot Springs, Yellowstone National Park, U.S.A.). *J. Sed. Res.* **2000**, *70*, 565–585. [CrossRef] [PubMed]
49. Renaut, R.W.; Jones, B.; Tiercelin, J.-J. Rapid in situ silicification of microbes at Loburu hot springs, Lake Bogoria, Kenya Rift Valley. *Sedimentology* **1998**, *45*, 1083–1103. [CrossRef]
50. Canet, C.; Prol-Ledesma, R.M.; Torres-Alvarado, I.; Gilg, H.A.; Villanueva, R.E.; Lozano-Santa Cruz, R. Silica-carbonate stromatolites related to coastal hydrothermal venting in Bahía Concepción, Baja California Sur, Mexico. *Sediment. Geol.* **2005**, *174*, 97–113. [CrossRef]
51. Hua, Q.; Barbetti, M.; Rakowski, A.Z. Atmospheric radiocarbon for the period 1950-2010. *Radiocarbon* **2013**, *55*, 2059–2072. [CrossRef]
52. Gat, J.R. Oxygen and hydrogen isotopes in the hydrologic cycle. *Annu. Rev. Earth Planet. Sci.* **1996**, *24*, 225–262. [CrossRef]
53. Göhring, A.; Mauder, M.; Vohberger, M.; Nehlich, O.; von Carnap-Bornheim, C.; Hilberg, V.; Kröger, P.; Grupe, G. Palaeobiodiversity research based on stable isotopes: Correction of the sea spray effect on bone carbonate $\delta^{13}C$ and $\delta^{18}O$ by Gaussian Mixture Model clustering. *Palaeogeogr. Palaeoclimatol. Palaeoecol.* **2018**, *490*, 673–686. [CrossRef]
54. Deininger, M.; Fohlmeister, J.; Scholz, D.; Mangini, A. Isotope disequilibrium effects: The influence of evaporation and ventilation effects on the carbon and oxygen isotope composition of speleothems—A model approach. *Geochim. Cosmochim. Acta* **2012**, *96*, 57–79. [CrossRef]
55. Yan, H.; Liu, Z.; Sun, H. Large degrees of carbon isotope disequilibrium during precipitation-associated degassing of CO_2 in mountain stream. *Geochim. Cosmochim. Acta* **2020**, *273*, 244–256. [CrossRef]
56. Beeler, S.R.; Gomez, F.J.; Bradley, A.S. Controls of extreme isotopic enrichment in modern microbialites and associated abiogenic carbonates. *Geochim. Cosmochim. Acta* **2020**, *269*, 136–149. [CrossRef]
57. Leng, M.J.; Marshall, J.D. Palaeoclimate interpretation of stable isotope data from lake sediment archives. *Quat. Sci. Rev.* **2004**, *23*, 811–831. [CrossRef]
58. Talbot, M.R. A review of the palaeohydrological interpretation of carbon and oxygen isotopic ratios in primary lacustrine carbonates. *Chem. Geol. Isot. Geosci. Sect.* **1990**, *80*, 261–279. [CrossRef]
59. Pueyo, J.J.; Sáez, A.; Giralt, S.; Valero-Garcés, B.L.; Moreno, A.; Bao, R.; Schwalb, A.; Herrera, C.; Klosowska, B.; Taberner, C. Carbonate and organic matter sedimentation and isotopic signatures in Lake Chungará, Chilean Altiplano, during the last 12.3 kyr. *Palaeogeogr. Palaeoclimatol. Palaeoecol.* **2011**, *307*, 339–355. [CrossRef]

Publisher's Note: MDPI stays neutral with regard to jurisdictional claims in published maps and institutional affiliations.

© 2020 by the authors. Licensee MDPI, Basel, Switzerland. This article is an open access article distributed under the terms and conditions of the Creative Commons Attribution (CC BY) license (http://creativecommons.org/licenses/by/4.0/).